nature neuroscience

ARTICLES

https://doi.org/10.1038/s41593-022-01049-x

Neuronal activity drives pathway-specific depolarization of peripheral astrocyte processes

Moritz Armbruster[1]✉, Saptarnab Naskar[1], Jacqueline P. Garcia[1,2], Mary Sommer[1], Elliot Kim[1], Yoav Adam[3,11], Philip G. Haydon[1], Edward S. Boyden[4,5,6,7,8,9], Adam E. Cohen[3,10] and Chris G. Dulla[1]✉

Astrocytes are glial cells that interact with neuronal synapses via their distal processes, where they remove glutamate and potassium (K^+) from the extracellular space following neuronal activity. Astrocyte clearance of both glutamate and K^+ is voltage dependent, but astrocyte membrane potential (V_m) is thought to be largely invariant. As a result, these voltage dependencies have not been considered relevant to astrocyte function. Using genetically encoded voltage indicators to enable the measurement of V_m at peripheral astrocyte processes (PAPs) in mice, we report large, rapid, focal and pathway-specific depolarizations in PAPs during neuronal activity. These activity-dependent astrocyte depolarizations are driven by action potential-mediated presynaptic K^+ efflux and electrogenic glutamate transporters. We find that PAP depolarization inhibits astrocyte glutamate clearance during neuronal activity, enhancing neuronal activation by glutamate. This represents a novel class of subcellular astrocyte membrane dynamics and a new form of astrocyte–neuron interaction.

Astrocytes are glial cells with complex, ramified morphologies that enable their extensive physical interactions with synapses, blood vessels and other cells. Nanometer-scale astrocyte processes extend toward synaptic structures and are enriched in many functional astrocyte proteins. Excitatory amino acid transporters (EAATs; GLT1 and GLAST)[1], which remove extracellular glutamate and provide spatiotemporal control of excitatory neurotransmission, are concentrated in perisynaptic astrocyte processes. Likewise, the inward rectifying potassium (K^+) channel Kir4.1 is present at the fine processes where astrocytes contact synapses[2], helping to restore extracellular [K^+] after neuronal activity. EAAT function is strongly inhibited at depolarized membrane potentials[1], but whole-cell recordings from astrocyte soma show that V_m changes very little during neuronal activity (but see refs. [3,4] for larger changes reported in vivo during synchronous activity and seizures). This has led to the assumption that astrocytes are electrically passive and undergo only very small changes in V_m. However, because astrocytes have very low membrane resistance (R_m), there is minimal spatial propagation of depolarization[5] and astrocyte morphology renders most of the astrocyte arbor inaccessible to electrophysiological recording. Therefore, we have no direct understanding of how V_m changes outside of the astrocyte soma during neuronal activity. We suspected that astrocyte V_m in the processes might be more dynamic than previously appreciated because EAAT function, which is reduced by membrane depolarization, is rapidly and reversibly inhibited by short bursts of neuronal activity[6,7]. Here we use genetically encoded voltage indicators (GEVIs) to demonstrate that neuronal activity induces large, rapid, focal and pathway-specific depolarizations in PAPs. Electron microscopy shows that astrocyte processes that directly interact with neuronal synaptic structures are ≈100 nm, below our resolution limits, so we use the term PAP to broadly reference the fine astrocyte processes outside of astrocytic soma and primary processes. With that caveat in mind, we find that neuronal activity induces PAP depolarization primarily via elevated extracellular K^+, with glutamate transport playing a smaller, secondary role. Activity-induced PAP depolarizations inhibit glutamate transporter function, thereby increasing excitatory *N*-methyl-D-aspartate (NMDA) receptor-mediated neurotransmission onto cortical pyramidal neurons. Activity-induced PAP depolarizations represent a novel form of astrocyte–neuron communication and have important implications in understanding the role of astrocytes in shaping extracellular glutamate and K^+ dynamics. We anticipate that this finding will motivate further study of how V_m modulates other astrocyte processes and how injury, inflammation and disease alter this fundamental aspect of astrocyte function.

Results

GEVIs show fast activity-dependent astrocyte depolarization. We expressed the GEVIs Archon1-EGFP[8] and Arclight[9] in layer II/III mouse cortical astrocytes using adeno-associated virus (AAV)-mediated transduction under the control of a modified glial fibrillary acidic protein (GFAP) promoter[10]. Immunohistochemical studies show that robust GEVI expression colocalized with the astrocyte marker glutamine synthase (GS), but not with the neuronal marker NeuN (Fig. 1a,b). Transduced astrocytes were morphologically reconstructed (AAV5-GFAP-tdTomato or EAAT2-tdTomato mice[11]) and GEVI expression was seen throughout the astrocyte

[1]Department of Neuroscience, Tufts University School of Medicine, Boston, MA, USA. [2]Cell, Molecular, and Developmental Biology Program, Tufts Graduate School of Biomedical Sciences, Boston, MA, USA. [3]Department of Chemistry and Chemical Biology, Harvard University, Cambridge, MA, USA. [4]Department of Brain and Cognitive Sciences, Massachusetts Institute of Technology, Cambridge, MA, USA. [5]Department of Biological Engineering, Massachusetts Institute of Technology, Cambridge, MA, USA. [6]McGovern Institute, Massachusetts Institute of Technology, Cambridge, MA, USA. [7]Howard Hughes Medical Institute, Massachusetts Institute of Technology, Cambridge, MA, USA. [8]Koch Institute, Massachusetts Institute of Technology, Cambridge, MA, USA. [9]Center for Neurobiological Engineering, Massachusetts Institute of Technology, Cambridge, MA, USA. [10]Department of Physics, Harvard University, Cambridge, MA, USA. [11]Present address: Edmond and Lily Safra Center for Brain Sciences, the Hebrew University of Jerusalem, Jerusalem, Israel. ✉e-mail: Moritz.Armbruster@tufts.edu; Chris.Dulla@tufts.edu

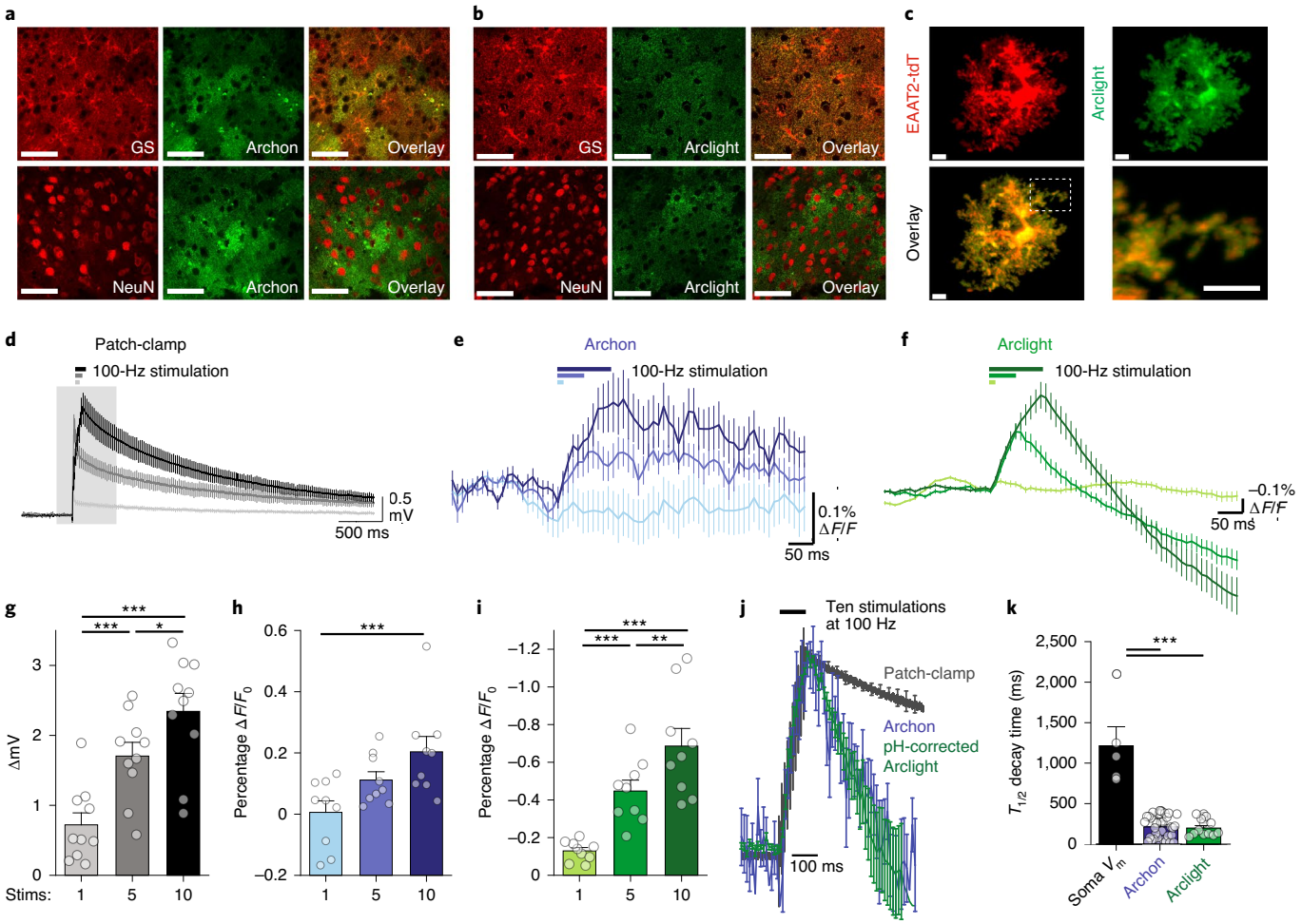

Fig. 1 | Astrocyte GEVI imaging enables measurement of astrocyte PAP V_m changes. a,**b**, Immunohistochemistry images of astrocyte expression of GEVIs Archon (AAV5-GFAP-Archon, **a**) and Arclight (AAV5-GFAP-Arclight, **b**), showing astrocyte-specific expression with colocalization with GS but absence of colocalization with NeuN. Scale bars, 50 µm; repeated for three mice under each condition. **c**, Astrocyte reconstruction based on the astrocyte reporter line EAAT2-tdTomato, showing that Arclight GEVI labels the full astrocytic arbor. Scale bars, 5 µm (inset, 5 µm) (see Extended Data Fig. 2 for additional reconstructions). **d**–**f**, Whole-cell current-clamp recordings (**d**) of astrocyte ΔV_m in response to one, five or ten stimuli (stims) at 100 Hz. Gray box marks time scale for astrocyte GEVI responses to the same stimuli for Archon (**e**) and Arclight (**f**). **g**–**i**, Whole-cell recording (**g**) of Archon (**h**) and Arclight (**i**) showing progressive depolarizations for increased stimulus number at 100 Hz. One-way repeated-measures ANOVA and Tukey's post test: **g**, one versus five stimuli, $P = 2.1 \times 10^{-4}$; one versus ten stimuli, $P = 3.1 \times 10^{-7}$; five versus ten stimuli, $P = 0.010$; **h**, one versus five stimuli, $P = 0.051$; one versus ten stimuli, $P = 5.3 \times 10^{-4}$; five versus ten stimuli, $P = 0.093$; **i**, one versus five stimuli, $P = 7.7 \times 10^{-4}$; one versus ten stimuli, $P = 1.3 \times 10^{-6}$; five versus ten stimuli, $P = 0.0083$). **j**,**k**, Normalized overlay of ten-stimulus, 100-Hz responses (**j**) of patch-clamp, Archon and Arclight pH-corrected decays showing significantly faster decay for GEVI assays compared to patch-clamp (**k**). $n = 5$ cells per three mice (patch-clamp), $n = 33$ slices per eight mice (Archon), $n = 11$ slices per three mice (Arclight). One-way ANOVA and Tukey's post test: soma V_m versus Archon, $P < 1 \times 10^{-11}$; soma V_m versus Arclight, $P < 1 \times 10^{-11}$; Archon versus Arclight, $P = 0.98$. $^*P < 0.05$, $^{**}P < 0.01$, $^{***}P < 0.001$. Error bars denote s.e.m.

arbor (Fig. 1c and Extended Data Figs. 1 and 2). Transduced astrocytes showed low GFAP expression and were morphologically similar to untransduced astrocytes, consistent with minimal reactive astrogliosis (Extended Data Figs. 1 and 2). This confirms that our approach enables the imaging of V_m throughout the astrocyte arbor.

Acute coronal brain slices were then prepared, and somatic whole-cell recordings were made from layer II/III astrocytes while ascending cortical axons were activated via electrical stimulation (one, five or ten stimuli at 100 Hz). Consistent with previous reports, small somatic depolarizations were seen with stimulation (Fig. 1d). The amplitude of somatic depolarization increased with the number of stimuli delivered. Next, GEVI imaging of layer II/II astrocytes was performed using spinning-disk confocal microscopy. Stimulus-evoked changes in astrocyte GEVI fluorescence intensity ratio ($\Delta F/F_0$) were quantified, with both Archon1 and Arclight showing stimulus-evoked changes in $\Delta F/F_0$, consistent with astrocytic depolarization (Archon1: ↑ $\Delta F/F_0$, Arclight: ↓ $\Delta F/F_0$, depolarization). GEVI $\Delta F/F_0$ amplitude increased with stimulus number (Fig. 1e,f,h,i) similarly to somatic electrophysiological recordings of V_m.

We next examined the decay time of activity-induced astrocyte depolarizations monitored using GEVIs, versus those recorded electrophysiologically at the soma. Because Arclight is based on pHluorin it undergoes pH-dependent quenching of fluorescence[12], interfering with quantification of ΔV_m kinetics. To correct this pH effect, pHluorin quenching was imaged in separate experiments using a cytosolic-facing, membrane-targeted pHluorin construct (AAV5-GFAP-Lyn-mCherry-pHluorin)[13], mimicking pHluorin's position in the Arclight construct. pHluorin imaging revealed pH-dependent changes in $\Delta F/F_0$ that were used to correct Arclight

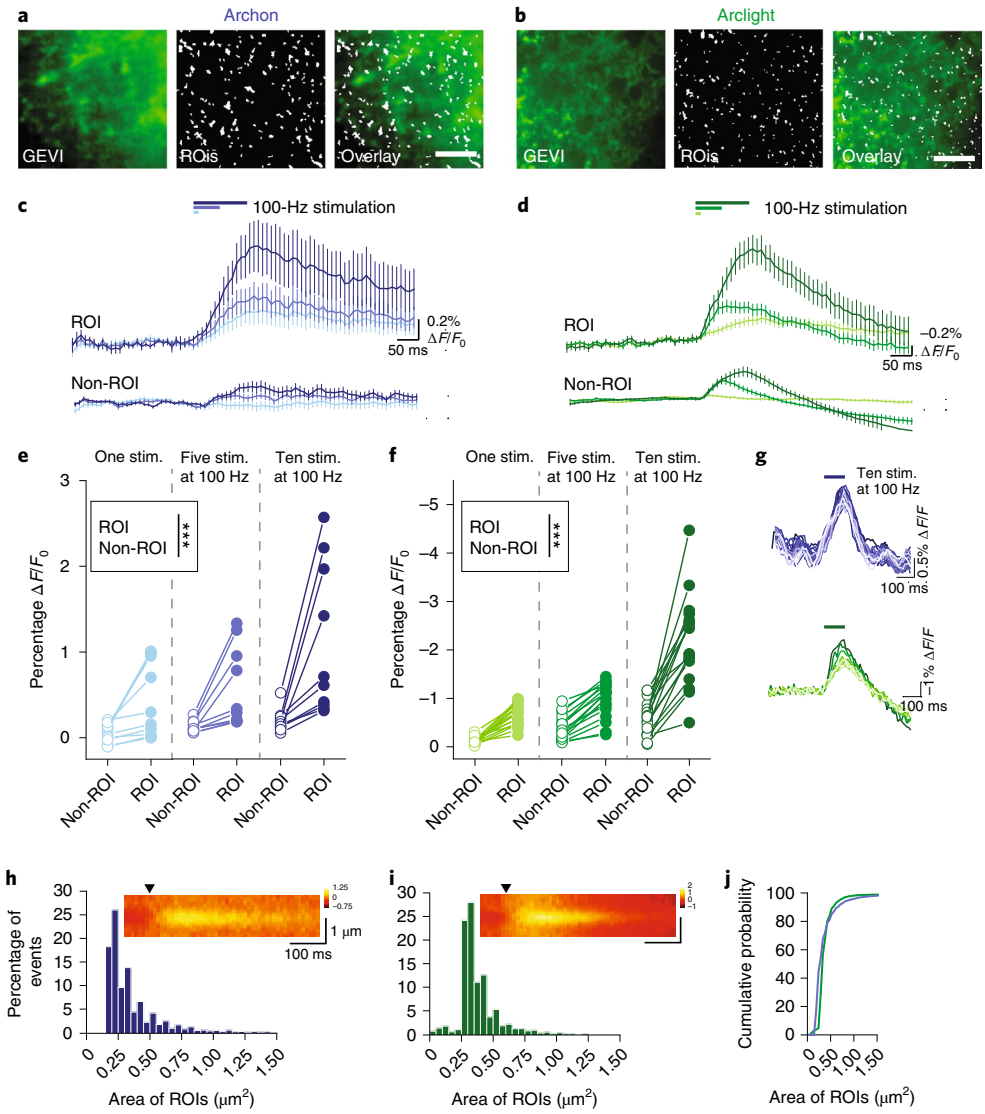

Fig. 2 | Astrocyte GEVI shows microdomain depolarizations. a, Responses of Archon GEVI colabel (GFP) and ROI maps based on ten stimuli at 100 Hz, showing small and distributed ROIs. **b**, Arclight (basal fluorescence) and ROI maps showing small and distributed ROIs. Scale bars, 10 μm. **c**,**d**, Average traces of ROI and non-ROI regions from Archon (**c**) and Arclight (**d**) in response to one, five and ten stimuli at 100 Hz. **e**,**f**, Archon (**e**) and Arclight (**f**) ROIs showing significantly enhanced responses ($\Delta F/F_0$). $n = 10$ slices per five mice (Archon), $n = 17$ slices per six mice (Arclight). Two-way repeated-measures ANOVA, Tukey's post test Archon ROI versus non-ROI $P = 9.9 \times 10^{-5}$; Arclight ROI versus non-ROI $P = 6.3 \times 10^{-8}$, $^{***}P < 0.001$. **g**, Single-slice examples of repeated ten-stimulus, 100-Hz trains showing stable GEVI responses across multiple rounds of stimulation. **h**,**i**, Distribution of ROI size for Archon (**h**) and Arclight (**i**) showing small responsive areas, and average kymographs showing spatially restricted areas of depolarization. Black arrowheads indicate time of stimulation. **j**, Both GEVIs showing similar size distribution. Error bars represent s.e.m.

signals for changes in pH (Extended Data Fig. 3). Both Archon1 and pH-corrected Arclight showed ΔV_m $T_{1/2}$ decay times of approximately 200 ms (Archon, $T_{1/2} = 211.2 \pm 24.3$ ms, $n = 33$ slices per eight mice; Arclight, $T_{1/2} = 197.3 \pm 30.9$ ms, $n = 11$ slices per three mice), while $T_{1/2}$ decay times for depolarization measured with somatic whole-cell recording were ≈fivefold slower (1,206.8 ± 234.7 ms, $n = 5$ cells per three mice, Fig. 1j,k). This suggests that voltage changes measured using GEVIs have kinetic properties distinct from those measured electrophysiologically at the soma. Because most of the astrocyte membrane is found in processes, membrane-targeted probes predominantly report activity in astrocyte processes[14]. In fact, confocal imaging shows that only ≈1% of Arclight fluorescence originates from the astrocyte soma (Extended Data Fig. 4). Therefore, we suspected that GEVI signal may be heavily biased toward astrocyte process V_m.

Astrocyte depolarizations are focal and spatially stable. We next used principal component analysis/independent component analysis (PCA/ICA)[15] to identify regions of depolarization in astrocytes using both Archon1 and Arclight. This identified small 'hotspots' that were used as regions of interest (ROIs) for GEVI analysis (Fig. 2a,b, Supplementary Figs. 1 and 2 and Supplementary Methods). Stimulus-evoked $\Delta F/F_0$ in these hotspots was significantly enhanced compared with all other regions within the imaged area (Fig. 2c–f), and was stable over repeated trials (Fig. 2g). Detected ROIs were extremely focal (Archon: 0.36 ± 0.02 μm², $n = 10$ slices per five mice; Arclight: 0.49 ± 0.15 μm², $n = 17$ slices per six mice), with similar size distribution for both GEVIs (Fig. 2h–j), suggesting they may have originated from PAPs. Kymographs also confirmed spatially restricted depolarizations (Arclight: full width at half maximum (FWHM) = 446 ± 7 nm, $n = 8$

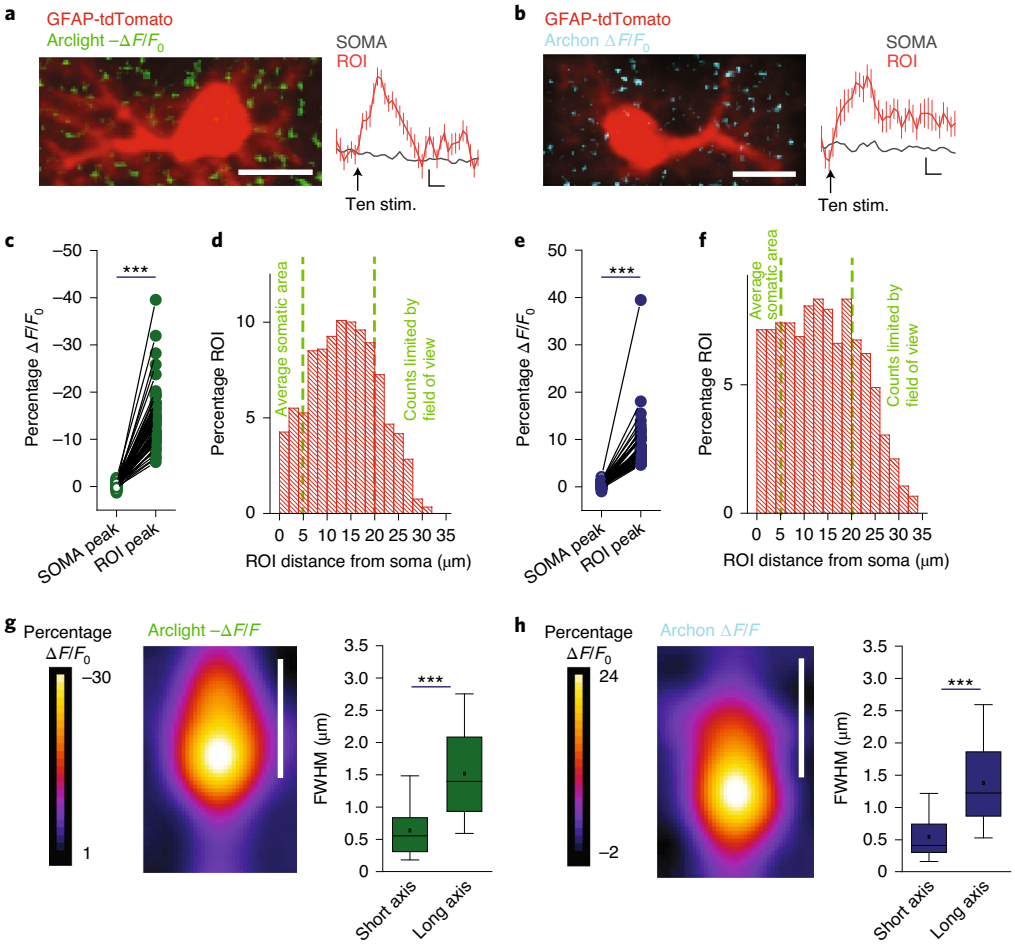

Fig. 3 | Astrocyte GEVI depolarization microdomains occur outside of astrocyte somas and primary processes. a, Arclight GEVI coexpressed with GFAP-tdTomato to label astrocyte soma and primary processes. Example image of Arclight $-\Delta F/F_0$ in response to ten stimuli at 100 Hz, showing that hotspots localize outside of astrocyte soma and primary processes. Example trace of single slice showing Arclight ROI and soma response. Scale bar, 10 μm (trace scale bars, −2% $\Delta F/F_0$, 200 ms). **b**, Archon GEVI coexpressed GFAP-tdTomato as in **a**. Example image of Archon $\Delta F/F_0$ hotspots localized outside of astrocyte soma and primary processes. Example trace of Archon response of ROI and soma. Scale bar, 10 μm (trace scale bars, 2% $\Delta F/F_0$, 200 ms). **c**, Peak Arclight $-\Delta F/F_0$ response showing significantly enhanced response of ROIs compared with soma. Paired *t*-test, $n = 59$ astrocytes from four mice, $P = 3.1 \times 10^{-24}$. **d**, Histogram of Arclight ROI distances from soma center of mass, showing broad distribution of ROIs throughout the astrocyte arbor. **e**, Peak Archon $\Delta F/F_0$ response showing significantly enhanced response of ROIs compared with soma. Paired *t*-test, $n = 47$ astrocytes from three mice, $P = 1.4 \times 10^{-14}$. **f**, Histogram of Archon ROI distances from soma center of mass, showing broad distribution of ROIs throughout the astrocyte arbor. **g**, Arclight ROIs are aligned and overlayed and peak ROI visualized; ROIs showing asymmetry with long and short axes. Scale bar, 1 μm, 432 ROIs from four mice, $P = 9.2 \times 10^{-107}$. **h**, Archon ROIs are aligned and overlayed and peak ROI visualized; ROIs showing asymmetry with long and short axes; 530 ROIs from three mice. Paired two-sample *t*-test, $P = 1.3 \times 10^{-128}$, $^{***}P < 0.001$. Box-and-whisker plots: box represents 25th, 50th and 75th percentile, whiskers 5th–95th percentile and squares represent mean.

slices per five mice; Archon: FWHM = 572 ± 17 nm, $n = 9$ slices per four mice; Fig. 2h–i). These spatial measurements reflect a combination of depolarization size, the spatial size of astrocyte processes and the optical limitations of our microscopy approaches. As a result, our estimates of GEVI hotspot FWHM are probably an overestimate of the physical size of the underlying depolarization but are consistent with depolarization originating from PAPs.

To identify the location of activity-induced GEVI hotspots within the astrocyte arbor, we coinfected GEVIs with AAV5-GFAP-tdTomato to fluorescently identify astrocyte soma and primary processes. Additionally, we switched imaging modalities to a confocal line-scanning microscope with improved confocality by avoiding the pinhole crosstalk that occurs in spinning-disk microscopy. Using this approach, we discovered that GEVI hotspots are found primarily outside of the astrocyte soma and primary processes (Fig. 3a,b). A small number of hotspots were located on soma/primary processes, but we suspect these represent closely coincident fine processes[14] that cannot be resolved at our axial/spatial resolution. Consistent with astrocyte PAP depolarizations, GEVI signal was significantly enhanced in hotspot ROIs compared with ROIs containing the astrocyte soma and primary processes (Fig. 3c,e). When we examined the spatial distribution of GEVI hotspots, we found that they were broadly distributed across the astrocyte arbor (Fig. 3d,f), again consistent with PAP depolarizations.

To further understand hotspot morphology, we quantified their individual spatial properties. Interestingly, hotspots were asymmetrical with a long and a short axis (Fig. 3 and Extended Data Fig. 5). We created an average GEVI hotspot profile by aligning individual hotspots along their long axis. We found that GEVI hotspots were small and asymmetrical (FWHM: Arclight, 637 ± 20 nm short

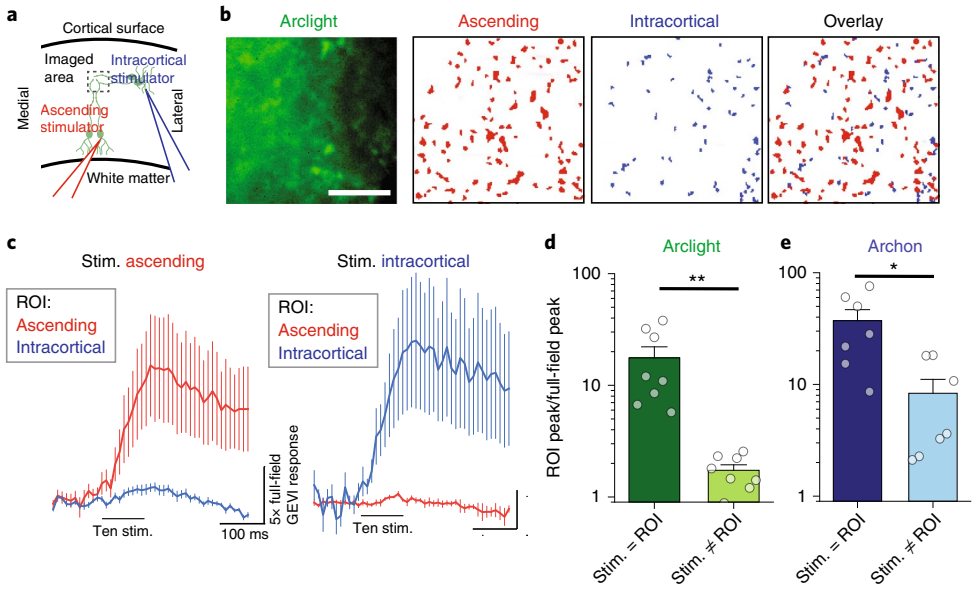

Fig. 4 | Pathway independence of astrocyte depolarization. a, To test pathway specificity we utilized an ascending stimulator (red) and an intracortical stimulator (blue). **b**, Example ROI maps of ascending and intracortical stimulators showing little overlap. Scale bar, 10 µm. **c**, Average Arclight traces of matched ROI (stim., ascending and ROI, ascending), (stim., intracortical and ROI, intracortical) or unmatched. **d**,**e**, Arclight (**d**) and Archon (**e**) matched ROIs showing significant enhancement of PAP $\Delta F/F_0$ over unmatched, suggesting pathway specificity, log scale; $n = 8$ slices per three mice (Arclight, $P = 0.0033$), $n = 7$ slices per three mice (Archon, $P = 0.021$), paired t-test, $^*P < 0.05$, $^{**}P < 0.01$. Error bars represent s.e.m.

dimension and 1,518 ± 34 nm long dimension; Archon, 545 ± 15 nm short dimension and 1,380 ± 29 nm long dimension; Fig. 3g,h). The small dimensions of the hotspot FWHM were similar to what was observed with spinning-disk imaging, where rotational alignment was not possible due to signal to noise. The large dimension probably occurs due to a spatial spread of depolarization along PAPs and is consistent with an astrocyte membrane space constant of ~3 µm[5,16]. We fit individual ROI hotspots to calculate their spatial properties along both axes, and found that hotspots were significantly more skewed along the long axis (y axis) (Extended Data Fig. 5). This is in line with depolarization initiating at the tip of astrocyte processes and spreading unidirectionally along the long axis. Given the limitations of our spatial resolution and the size of astrocyte fine processes, however, new approaches will need to be developed to conclusively determine the precise subcellular and subprocess localization of astrocyte depolarizations within PAPs.

Astrocyte depolarizations are pathway specific. We next performed Arclight GEVI imaging using our standard high-speed, spinning-disk confocal approach while delivering electrical stimulation to either ascending cortical axons or L II/III intracortical axons (Fig. 4a)[6]. Hotspots were identified for each stimulation pathway using PCA/ICA. Interestingly, there was minimal spatial overlap of astrocyte depolarization hotspots evoked by ascending and intracortical axons (Fig. 4b). ROIs identified from stimulation of ascending axons showed minimal responses when intracortical axons were stimulated, and vice versa (Fig. 4c,d). Archon1 imaging replicated the pathway-specific enrichment of $\Delta F/F_0$ results (Fig. 4e). Together, this demonstrates that stimulus-induced astrocyte depolarization is pathway specific and could provide a mechanism to drive synapse-specific modulation of glutamate uptake and other astrocyte functions[6].

Calibration of GEVI signal in PAPs. We next estimated ΔV_m associated with $\Delta F/F_0$ using a straightforward calibration approach. This and subsequent experiments were performed using exclusively Arclight, due to its better signal-to-noise characteristics in our assay. In separate experiments we measured astrocyte somatic V_m using electrophysiology and PAP GEVI fluorescence while increasing $[K^+]$ in the extracellular solution. This should induce a spatially uniform depolarization of both astrocyte processes (Extended Data Fig. 6) and soma. As predicted, increasing extracellular $[K^+]$ depolarized somatic V_m (Fig. 5a) and altered GEVI fluorescence (Fig. 5b). We performed a linear fit of Arclight $\Delta F/F_0$ and somatic ΔV_m in response to increasing extracellular $[K^+]$, by 5 and 10 mM, respectively (linear fit with fixed intercept, $R^2 = 0.988$). Using this calibration, we estimate that $\Delta F/F_0$ seen in PCA/ICA-identified hotspots reflects depolarizations of 19.2 ± 2.1 mV in response to ten stimuli at 100 Hz, approximately tenfold more than seen at the soma (Fig. 1d). The same calibration approach suggests that non-hotspot regions depolarize by 5.1 ± 0.8 mV ($n = 17$ slices per six mice).

Presynaptic activity drives astrocyte depolarization via K^+_e and EAATs. To determine the mechanisms that drive PAP depolarization, we probed the effects of neuronal activity, postsynaptic glutamate receptor activity, EAAT activity and modulation of K^+ homeostasis on GEVI $\Delta F/F_0$. Tetrodotoxin (TTX), which blocks voltage-gated sodium channels, eliminated stimulus-evoked GEVI $\Delta F/F_0$, confirming that neuronal activity is required (Fig. 6a). This also eliminated the possibility that electrical stimulation acts directly on PAPs to drive their depolarization. We next assayed the role of glutamate receptor activation in PAP depolarization by blocking both AMPA and NMDA receptors (DNQX 20 µM and AP-5 50 µM, respectively). This had no effect on GEVI $\Delta F/F_0$, showing that activation of both AMPA and NMDA receptors does not contribute to PAP depolarization in this setting (Fig. 5b). Next, we tested whether EAAT-mediated glutamate uptake, which carries an inward, depolarizing current, contributes to activity-induced PAP depolarization. Blockage of EAATs with TFB-TBOA (1 µM) partially reduced GEVI $\Delta F/F_0$ (Fig. 6c). Interestingly, the effect of EAAT blockade was similar for both five and ten stimuli (Fig. 6g), consistent with suppression of glutamate release during prolonged trains of neuronal activity[6,7]. This also suggests that other mechanisms drive the increase in GEVI $\Delta F/F_0$ seen with increasing number of stimuli.

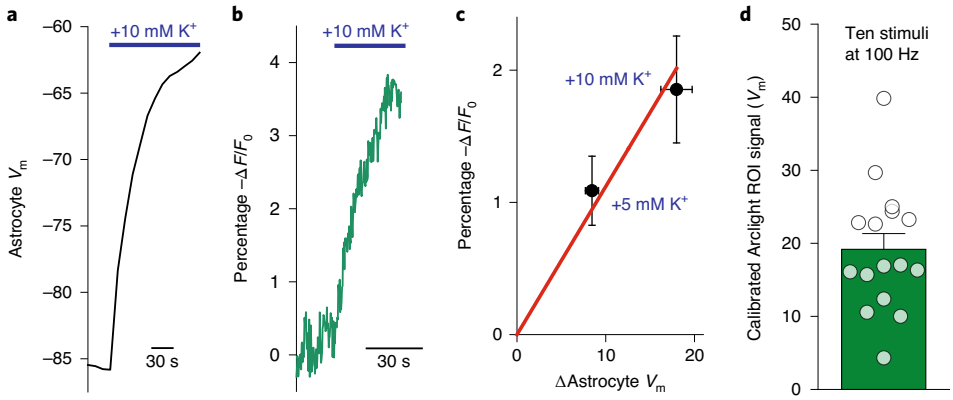

Fig. 5 | Calibration of Arclight GEVI. a,**b**, Example traces of astrocyte whole-cell recordings (**a**) and Arclight GEVI (**b**), showing depolarizations in control (2.5 mM K^+ aCSF) and in response to the addition of high K^+ to aCSF (+10 mM K^+). **c**, Correlation between whole-cell ΔV_m changes and Arclight $\Delta F/F_0$ in response to the addition of +5 and +10 mM K^+ to aCSF solutions, and fit with the line passing through the origin (red). Arclight, $n = 7$ slices per three animals per condition; whole-cell, $n = 8$ cells per three animals per condition. **d**, Arclight fluorescence peak ROI response to ten stimuli at 100 Hz mapped to ΔV_m using the calibration; $n = 17$ slices per six mice. Error bars denote s.e.m.

Because astrocyte V_m is highly dependent on $[K^+]_e$ and neuronal activity increases $[K^+]_e$ (ref. [17]), we tested whether manipulation of astrocyte K^+ handling would alter activity-dependent PAP depolarization. Kir4.1, the astrocytic inwardly rectifying K^+ channel, is the primary mediator of activity-dependent astrocyte K^+ buffering[18] and can be blocked with 200 µM Ba^{2+} (ref. [19]). Viral overexpression of Kir4.1 (Kir4.1-OE)[20–22] (AAV5-GFAP-Kir4.1-mCherry or AAV5-GFAP-Kir4.1-EGFP; Extended Data Fig. 7) significantly reduced GEVI $\Delta F/F_0$ for both five and ten stimuli (Fig. 6d). Unlike the effects of EAAT inhibition, the effect size of Kir4.1 overexpression on GEVI $\Delta F/F_0$ was significantly larger for ten as compared to five stimuli (Fig. 6g). Conversely, inhibition of Kir4.1 with Ba^{2+} caused a small but significant increase in GEVI $\Delta F/F_0$ (Fig. 6e), suggesting that Kir4.1-mediated K^+ influx helps minimize activity-dependent PAP depolarization. Conversely, Ba^{2+} blockade of Kir4.1 reduces stimulus-evoked depolarization of the soma as measured via whole-cell electrophysiology[18,23] (Extended Data Fig. 8). We next tested whether the effects of Kir4.1-OE and TFB-TBOA were additive. TFB-TBOA reduced activity-dependent GEVI $\Delta F/F_0$ even when Kir4.1 was overexpressed, confirming that EAAT activity and changes in $[K^+]_e$ represent distinct mechanisms contributing to PAP depolarization. This suggests that activity-dependent accumulation of extracellular K^+ is the primary driver of stimulus-dependent PAP depolarization, while EAAT activity plays a secondary role.

Finally, we asked whether reduction of extracellular Ca^{2+} (which can affect presynaptic function, membrane charge screening and Ca^{2+} signaling) would alter activity-dependent changes in GEVI $\Delta F/F_0$. Reduction of extracellular $[Ca^{2+}]$ from 2 to 1 mM had a strong effect on GEVI $\Delta F/F_0$ rise time, due to delayed onset of depolarization (sigmoidal $T_{1/2}$ rise time for ten stimuli at 100 Hz, 61.3 ± 3.6 ms; control, 85.1 ± 5.9 ms; low Ca^{2+}; paired *t*-test, $P = 0.0013$) and caused a small but significant decrease in PAP ΔV_m peak (Fig. 6h). While lowering of Ca^{2+} decreases glutamate release, glutamate receptor activation does not drive PAP depolarization (Fig. 6b) and low-Ca^{2+} effects on presynaptic release are not correlated with the effects on PAP depolarization (Extended Data Fig. 9). This suggests that activity-dependent changes in PAPs can be altered by lowering extracellular Ca^{2+}, but the precise mechanisms are unclear. We suspect that membrane charge screening[24] mediates the effects of lowered extracellular Ca^{2+} on PAP depolarization, but other potential mechanisms (Ca^{2+} signaling, Ca^{2+}-activated K^+ channels) also exist.

PAP V_m modulates glutamate clearance and NMDA receptor activation. The results we report suggests that voltage-dependent modulation of astrocyte function may occur in PAPs. Astrocyte glutamate clearance by EAATs is rapid (<10 ms)[25], steeply inhibited by depolarization in expression systems[1] and slowed by neuronal activity in cortical brain slices[6,7]. We therefore hypothesized that EAAT function may be modulated in astrocytes by activity-induced PAP depolarization. To test this hypothesis, we used approaches that alter activity-induced PAP GEVI $\Delta F/F_0$ (Fig. 6) and asked whether these manipulations affect the stimulus-dependent slowing of EAAT function and glutamate clearance. Using intensity-based, glutamate-sensing fluorescent reporter (iGluSnFr) glutamate imaging[6,26] and NR2A-specific NMDA currents[6], we tested the effects of low Ca^{2+} (Fig. 7a,b), Ba^{2+} (Fig. 7c,d) and Kir4.1-OE (Fig. 7e,f) on activity-dependent inhibition of glutamate clearance. Kir4.1-OE and low Ca^{2+}, which reduce PAP GEVI $\Delta F/F_0$ (Fig. 6d,h), both reduced the slowing of glutamate clearance associated with trains of neuronal activity. The slowing of glutamate clearance is independent of the amount of glutamate released[6] (Extended Data Fig. 9), suggesting that the effects of low Ca^{2+} are not mediated by reduced presynaptic glutamate release. Recording of astrocyte glutamate transporter currents (GTCs) confirmed that lowering of Ca^{2+} reduced activity-dependent inhibition of EAAT function (as assayed by GTC decay times; Extended Data Fig. 10). Conversely, blockage of Kir4.1 with Ba^{2+}, which augments PAP GEVI $\Delta F/F_0$ (Fig. 6e), enhanced the activity-dependent slowing of glutamate clearance (Fig. 7c,d). These experiments show that activity-dependent astrocyte depolarization inhibits EAAT function.

Discussion

Using GEVI imaging, we show that astrocytes undergo highly focal depolarizations ($\Delta V_m \approx 20$ mV) during brief bouts of neuronal activity. These depolarizations occur with pathway specificity, are driven by a combination of presynaptic K^+ release and EAAT activity and impact activity-induced slowing of glutamate uptake. These results challenge the view that astrocytes have largely invariant membrane potential, and show that local astrocyte depolarizations have functional effects on EAAT activity and glutamate neurotransmission. Our data support the premise that GEVI-detected changes in V_m occur largely in astrocyte PAPs, outside the astrocyte soma and primary processes. Although optical limitations prevent us from conclusively saying that GEVI hotspots represent astrocyte processes directly adjacent to synapses, multiple pieces of

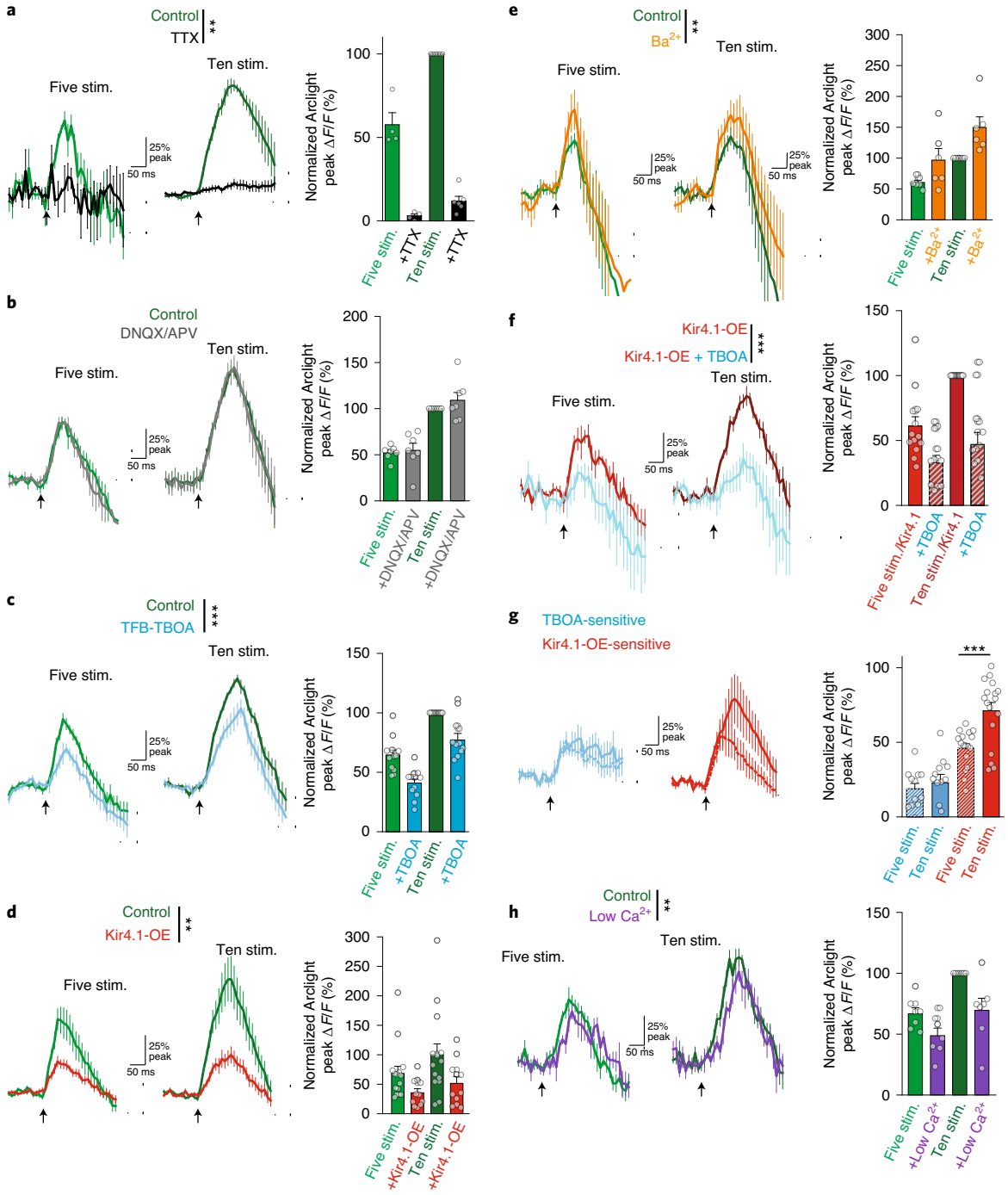

Fig. 6 | Glutamate transport and increases in $[K^+]_e$ contribute to astrocyte depolarization. a–h, Arclight GEVI imaging in response to five and ten stimuli at 100 Hz. **a**, TTX abolishes the GEVI response; $n=6$ slices per three mice, $P=1.3\times10^{-4}$. **b**, Postsynaptic glutamate receptors blockers DNQX and APV have no effect on peak GEVI response; $n=7$ slices per three mice, $P=0.89$. **c**, The EAAT inhibitor TFB-TBOA reduces peak GEVI signal for five and ten stimuli; $n=13$ slices per three mice, $P=6.9\times10^{-5}$. **d**, Kir4.1-OE significantly reduces GEVI depolarization peak; $n=15$ slices per five mice (control), $n=11$ slices per four mice (Kir4.1-OE), $P=0.0056$. **e**, Inhibition of Kir4.1 with 200 µM Ba^{2+} enhances GEVI signal; $n=6$ slices per three mice, $P=0.0041$. **f**, TFB-TBOA reduces Arclight GEVI peaks of Kir4.1-OE astrocytes, showing that effects are additive; $n=13$ slices per three mice, $P=9.9\times10^{-5}$. **g**, Average TFB-TBOA- and Kir4.1-OE-sensitive traces. TFB-TBOA-sensitive effect dis not increase from five to ten stimuli, while Kir4.1-OE-sensitive effects were enhanced with additional stimuli; paired *t*-test, $P=0.54$ and $P=3.7\times10^{-7}$, respectively. **h**, Reduction of extracellular Ca^{2+} reduces peak Arclight signal; $n=7$ slices per three mice, $P=0.0093$; two-way ANOVA and Tukey's post test, $^{***}P<0.001$; two-way repeated-measures ANOVA and Tukey's post test, $^{**}P<0.01$, $^{***}P<0.001$. Error bars denote s.e.m.

evidence suggest they do. Depolarizations are driven by both presynaptic neuronal activity and glutamate transport and shape synaptic glutamate dynamics. The spatial properties of activity-induced GEVI hotspots show that they are asymmetrical and are skewed along their long axis, consistent with depolarizations that initiate at the tips of astrocyte processes. Although these data suggest that

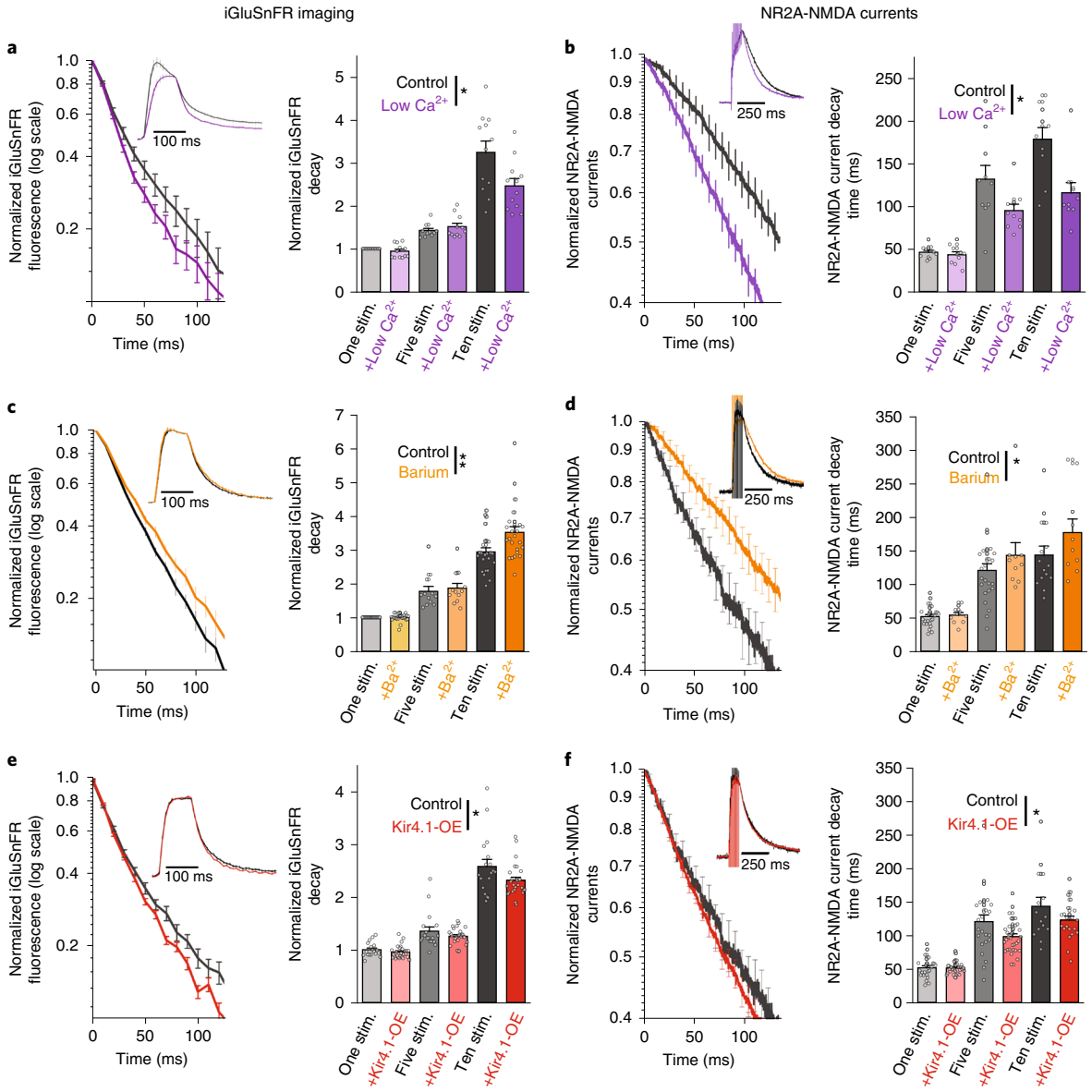

Fig. 7 | Astrocyte depolarization contributes to activity-dependent slowing of glutamate clearance. a–f, Glutamate clearance slowing, as assayed by single exponential fits to iGluSnFr imaging and NR2A-specific NMDA current decays in response to one, five and ten stimuli at 100 Hz. **a**, Low Ca^{2+} accelerates average iGluSnFr decay following ten stimuli at 100 Hz (inset, full trace); $n=12$ slices per five mice, $P=0.039$. **b**, Average ten-stimulus, 100-Hz NR2A-NMDA current decay showing that low Ca^{2+} aCSF speeds NR2A-NMDA current decay (inset, full trace); $n=10$ cells per three mice, $P=0.011$. **c**, Inhibition of Kir4.1 with 200 µM Ba^{2+} slows iGluSnFr decay; $n=24$ slices per six mice, $P=0.0086$. **d**, Inhibition of Kir4.1 with 200 µM Ba^{2+} prolongs NR2A-NMDA currents; $n=15$ cells per three mice (control), $n=10$ cells per four mice (Ba^{2+}), $P=0.026$. **e**, Kir4.1-OE accelerates iGluSnFr decay; $n=18$ slices per three mice (control), $n=27$ slices per four mice (Kir4.1-OE), $P=0.010$. **f**, Kir4.1-OE speeds NR2A-NMDA current decay; $n=33$ cells per four mice, control same as **d**, $P=0.046$, two-way ANOVA, $^{*}P<0.05$, $^{***}P<0.001$; two-way repeated-measures ANOVA $^{*}P<0.05$, $^{**}P<0.01$. Error bars denote s.e.m.

astrocyte depolarizations occur at processes adjacent to synapses, caveats of live imaging in nanometer-scale processes make this difficult to confirm using our current approaches. Additionally, multiple mechanisms contribute to the morphological properties of the PAP depolarizations we report, including the astrocyte membrane space constant (~3 µm[5,16]), the spatial relationship between astrocyte and neuronal processes, the location of K^+ release and K^+ diffusion in the extracellular space. Our results, therefore, may overestimate the spatial extent of PAP depolarization (FWHM ≈ 500 nm; Figs. 2h,i and 3g,h and Extended Data Fig. 5), and underestimate their peak amplitude. These caveats aside, our findings show that astrocytes undergo large, rapid and focal voltage changes during neuronal activity.

Elevation of $[K^+]_e$ appears to be a significant driver of activity-induced PAP depolarization. Astrocyte V_m is largely set by $[K^+]_e$, but the spatial nature of $[K^+]_e$ dynamics is not well understood. Our findings predict that neuronal activity induces highly focal increases in $[K^+]_e$ in the magnitude of ≈10 mM in response to neuronal electrical stimulation. This is significantly larger than generally reported during brief bursts of neuronal activity, but the small spatial scale of the predicted elevations in $[K^+]_e$ would be difficult to resolve using previous approaches such as K^+-selective electrodes. During prolonged activity (>30 s) or pathological states, like seizures, $[K^+]_e$ can increase to ≈10 mM, making our reported measurement physiologically possible[17,27]. The small spatial nature of

the depolarizations we report may have important implications for astrocytic K^+ buffering. Locally elevated $[K^+]_e$ depolarizes astrocytes, as modeled by the Nernst potential/Goldman–Hodgkin–Katz equation. Because Kir4.1-mediated K^+ influx helps $[K^+]_e$ levels return to baseline, astrocyte V_m locally recovers and, therefore, blockage of Kir4.1 enhances PAP depolarizations (Fig. 6), presumably by increasing and prolonging activity-induced changes in $[K^+]_e$. At the soma, because $[K^+]_e$ changes very little (Fig. 3 and Extended Data Fig. 8), small, slow somatic astrocyte depolarization is probably driven by Kir4.1-mediated inward K^+ currents occurring throughout the cell, rather than by local Nernstian-driven depolarization. In this situation, inhibition of Kir4.1 blocks the depolarizing inward current and reduces activity-induced astrocyte depolarization measured at the soma[18,23] (Extended Data Fig. 8). Future development of K^+_e imaging approaches and computational modeling of astrocytes[16] will continue to improve our understanding of the focal and dynamic nature of activity-induced astrocyte depolarization and astrocytic K^+ buffering.

Astrocytic glutamate uptake by EAATs is voltage dependent and inhibited by neuronal activity. Our data support the premise that PAP V_m shapes EAAT function during neuronal activity. Modulation of PAP V_m, by alteration of $[K^+]_e$ handing, can bidirectionally shape extracellular glutamate dynamics and NMDA receptor decay times. Alterion of PAP V_m has a significant, but relatively small, effect on EAAT function, suggesting that either our manipulations do not sufficiently control PAP V_m or that other changes (EAAT trafficking[28], cell swelling, diffusion or pH changes) play a key role in activity-dependent inhibition of EAAT function. We are unable to depolarize PAPs to directly test the correlation of glutamate clearance slowing and depolarization, due to technical limitations (small astrocyte space clamp and confounding ionic changes due to EAAT dependence on Na^+, K^+ and H^+). As a result, modulations of V_m and glutamate clearance are limited to correlative changes. Interestingly, neither activity-dependent EAAT inhibition nor PAP depolarization relies on glutamate receptor activation. This is surprising, because postsynaptic NMDA receptor activation has been shown to mediate K^+ efflux, which should depolarize astrocytes[29]. This could represent ultrastructural differences in K^+ handling at PAPs and soma or brain-region-specific astrocyte–neuron interactions. Our findings could also have important implications for both astrocyte–neuron interactions and the potential role of astrocyte depolarization in activity-dependent synaptic plasticity[30].

How PAP depolarization affects other astrocytic functions remains to be seen, but astrocytes have complex intracellular Ca^{2+} signaling and express voltage-dependent ion channels[31–34], receptors[35] and transporters[36] that may be functionally modulated by V_m. Additionally, experimental manipulations such as channelrhodopsin can increase $[K^+]_e$ (ref. [37]) that may affect astrocyte V_m. Finally, astrocytes are highly dynamic, responding to injury, inflammation and more. If PAP properties are altered during reactive astrocytosis, the coupling between neuronal activity and astrocyte function may be altered, especially during behaviorally relevant bursts of neuronal activity in vivo. Together, this study shows that astrocytes experience rapid, focal and functionally relevant depolarizations during neuronal activity.

Online content

Any methods, additional references, Nature Research reporting summaries, source data, extended data, supplementary information, acknowledgements, peer review information; details of author contributions and competing interests; and statements of data and code availability are available at https://doi.org/10.1038/s41593-022-01049-x.

Received: 23 July 2021; Accepted: 14 March 2022;
Published online: 28 April 2022

References

1. Levy, L., Warr, O. & Attwell, D. Stoichiometry of the glial glutamate transporter GLT-1 expressed inducibly in a Chinese hamster ovary cell line selected for low endogenous Na^+-dependent glutamate uptake. *J. Neurosci.* **18**, 9620–9628 (1998).
2. Higashi, K. et al. An inwardly rectifying K(+) channel, Kir4.1, expressed in astrocytes surrounds synapses and blood vessels in brain. *Am. J. Physiol. Cell Physiol.* **281**, C922–C931 (2001).
3. Amzica, F. & Neckelmann, D. Membrane capacitance of cortical neurons and glia during sleep oscillations and spike-wave seizures. *J. Neurophysiol.* **82**, 2731–2746 (1999).
4. Amzica, F. In vivo electrophysiological evidences for cortical neuron-glia interactions during slow (<1 Hz) and paroxysmal sleep oscillations. *J. Physiol. (Paris)* **96**, 209–219 (2002).
5. Ma, B., Xu, G., Wang, W., Enyeart, J. J. & Zhou, M. Dual patch voltage clamp study of low membrane resistance astrocytes in situ. *Mol. Brain* **7**, 18 (2014).
6. Armbruster, M., Hanson, E. & Dulla, C. G. Glutamate clearance is locally modulated by presynaptic neuronal activity in the cerebral cortex. *J. Neurosci.* **36**, 10404–10415 (2016).
7. Pinky, N. F., Wilkie, C. M., Barnes, J. R. & Parsons, M. P. Region- and activity-dependent regulation of extracellular glutamate. *J. Neurosci.* **38**, 5351–5366 (2018).
8. Piatkevich, K. D. et al. A robotic multidimensional directed evolution approach applied to fluorescent voltage reporters. *Nat. Chem. Biol.* **14**, 352–360 (2018).
9. Jin, L. et al. Single action potentials and subthreshold electrical events imaged in neurons with a fluorescent protein voltage probe. *Neuron* **75**, 779–785 (2012).
10. Lee, Y., Messing, A., Su, M. & Brenner, M. GFAP promoter elements required for region-specific and astrocyte-specific expression. *Glia* **56**, 481–493 (2008).
11. Yang, Y. et al. Molecular comparison of $GLT1^+$ and $ALDH1L1^+$ astrocytes in vivo in astroglial reporter mice. *Glia* **59**, 200–207 (2011).
12. Miesenbock, G., De Angelis, D. & Rothman, J. Visualizing secretion and synaptic transmission with pH-sensitive green fluorescent proteins. *Nature* **394**, 192–195 (1998).
13. Koivusalo, M. et al. Amiloride inhibits macropinocytosis by lowering submembranous pH and preventing Rac1 and Cdc42 signaling. *J. Cell Biol.* **188**, 547–563 (2010).
14. Shigetomi, E. et al. Imaging calcium microdomains within entire astrocyte territories and endfeet with GCaMPs expressed using adeno-associated viruses. *J. Gen. Physiol.* **141**, 633–647 (2013).
15. Mukamel, E. A., Nimmerjahn, A. & Schnitzer, M. J. Automated analysis of cellular signals from large-scale calcium imaging data. *Neuron* **63**, 747–760 (2009).
16. Savtchenko, L. P. et al. Disentangling astroglial physiology with a realistic cell model in silico. *Nat. Commun.* **9**, 3554 (2018).
17. Heinemann, U. & Lux, H. D. Ceiling of stimulus induced rises in extracellular potassium concentration in the cerebral cortex of cat. *Brain Res.* **120**, 231–249 (1977).
18. Olsen, M. L. & Sontheimer, H. Functional implications for Kir4.1 channels in glial biology: from K^+ buffering to cell differentiation. *J. Neurochem.* **107**, 589–601 (2008).
19. Olsen, M. L., Higashimori, H., Campbell, S. L., Hablitz, J. J. & Sontheimer, H. Functional expression of Kir4.1 channels in spinal cord astrocytes. *Glia* **53**, 516–528 (2006).
20. Tong, X. et al. Astrocyte Kir4.1 ion channel deficits contribute to neuronal dysfunction in Huntington's disease model mice. *Nat. Neurosci.* **17**, 694–703 (2014).
21. Cui, Y. et al. Astroglial Kir4.1 in the lateral habenula drives neuronal bursts in depression. *Nature* **554**, 323–327 (2018).
22. Kelley, K. W. et al. Kir4.1-dependent astrocyte-fast motor neuron interactions are required for peak strength. *Neuron* **98**, 306–319 (2018).
23. Djukic, B., Casper, K. B., Philpot, B. D., Chin, L. S. & McCarthy, K. D. Conditional knock-out of Kir4.1 leads to glial membrane depolarization, inhibition of potassium and glutamate uptake, and enhanced short-term synaptic potentiation. *J. Neurosci.* **27**, 11354–11365 (2007).
24. Hille, B. *Ion Channels of Excitable Membranes* 3rd edn (Sinauer Associates, 2001).
25. Diamond, J. Deriving the glutamate clearance time course from transporter currents in CA1 hippocampal astrocytes: transmitter uptake gets faster during development. *J. Neurosci.* **25**, 2906–2916 (2005).
26. Marvin, J. et al. An optimized fluorescent probe for visualizing glutamate neurotransmission. *Nat. Methods* **10**, 162–170 (2013).
27. Raimondo, J. V., Burman, R. J., Katz, A. A. & Akerman, C. J. Ion dynamics during seizures. *Front. Cell. Neurosci.* **9**, 419 (2015).
28. Murphy-Royal, C. et al. Surface diffusion of astrocytic glutamate transporters shapes synaptic transmission. *Nat. Neurosci.* **18**, 219–226 (2015).
29. Shih, P. Y. et al. Retrograde synaptic signaling mediated by K^+ efflux through postsynaptic NMDA receptors. *Cell Rep.* **5**, 941–951 (2013).

30. Sancho, L., Contreras, M. & Allen, N. J. Glia as sculptors of synaptic plasticity. *Neurosci. Res.* **167**, 17–29 (2021).
31. Letellier, M. et al. Astrocytes regulate heterogeneity of presynaptic strengths in hippocampal networks. *Proc. Natl Acad. Sci. USA* **113**, E2685–E2694 (2016).
32. D'Ascenzo, M. et al. Electrophysiological and molecular evidence of L-(Cav1), N- (Cav2.2), and R- (Cav2.3) type Ca^{2+} channels in rat cortical astrocytes. *Glia* **45**, 354–363 (2004).
33. Sontheimer, H., Black, J. A. & Waxman, S. G. Voltage-gated Na^{+} channels in glia: properties and possible functions. *Trends Neurosci.* **19**, 325–331 (1996).
34. Wan, X. et al. Bimodal voltage dependence of TRPA1: mutations of a key pore helix residue reveal strong intrinsic voltage-dependent inactivation. *Pflug. Arch.* **466**, 1273–1287 (2014).
35. Lalo, U., Pankratov, Y., Kirchhoff, F., North, R. A. & Verkhratsky, A. NMDA receptors mediate neuron-to-glia signaling in mouse cortical astrocytes. *J. Neurosci.* **26**, 2673–2683 (2006).
36. Willford, S. L., Anderson, C. M., Spencer, S. R. & Eskandari, S. Evidence for a revised ion/substrate coupling stoichiometry of GABA transporters. *J. Membr. Biol.* **248**, 795–810 (2015).
37. Octeau, J. C. et al. Transient, consequential increases in extracellular potassium ions accompany channelrhodopsin2 excitation. *Cell Rep.* **27**, 2249–2261 (2019).

Methods

Animals. All animal protocols were approved by the Tufts Institutional Animal Care and Use Committee. Experiments used C57/Bl6 and EAAT2-tdTomato[11] mice. Approximately equal numbers of male and female mice were used for all experiments. Mice were housed under 12/12-h light/dark cycles at approximately 21 °C and 30–70% humidity.

AAV injection. C57BL/6 or EAAT2-tdTomato[11] male and female mice (P30-45) were stereotaxtically injected with appropriate AAVs for experiments in a single hemisphere, using three injection sites (coordinates): (1.25, 1.25, 0.5), (1.25, 2.25, 0.5) and (1.25, 3.25, 0.5) ($\lambda+x$, $+y$, $-z$) mm. Mice were anesthetized with isoflurane for surgery and virus was injected (1 µl per site (1:1 dilution with saline for single infection or 1:1 mix of viruses for coinfection, 0.15 µl min^{-1}) with ~5×10^9 gene copies per virus. Mice were housed under a 12/12-h light/dark cycle following surgery and were used for acute slice preparations 21–42 days following injection.

We thank L. Looger, V. Pieribone, B. Khakh and S. Grinstein for making available the plasmids and constructs used in this study (Supplementary Table 1 provides a full listing of viruses used).

Preparation of acute brain slices. Cortical brain slices were prepared from AAV-infected mice[6]. Mice were anesthetized with isoflurane, decapitated and brains rapidly removed and placed in ice-cold slicing solution containing (in mM): 2.5 KCl, 1.25 NaH_2PO_4, 10 $MgSO_4$, 0.5 $CaCl_2$, 11 glucose, 234 sucrose and 26 $NaHCO_3$, and equilibrated with 95% O_2/5% CO_2. Brains were glued to a Vibratome VT1200S (Leica Microsystems), and slices (400 µm thickness) were cut in coronal orientation. Slices were then placed in a recovery chamber containing artificial cerebrospinal fluid (aCSF) comprising (in mM): 126 NaCl, 2.5 KCl, 1.25 NaH_2PO_4, 1 $MgSO_4$, 2 $CaCl_2$, 10 glucose and 26 $NaHCO_3$ (equilibrated with 95% O_2/5% CO_2). Slices were allowed to equilibrate in aCSF at 32 °C for 1 h. For astrocyte whole-cell experiments, slices were loaded with sulforhodamine 101 (SR-101, 0.5 µm) in aCSF for 5 min at 32 °C before equilibration[38] and then allowed to return to room temperature before electrophysiology/imaging. Low-Ca^{2+} aCSF reduced [Ca^{2+}] to 1 mM and balanced divalents with increased [Mg^{2+}]. Mg^{2+} has a lesser charge screening effect than Ca^{2+}, so even equimolar replacement should have charge screening effects[39–41]. High-[K^+] (7.5 and 12.5 mM) aCSF solutions were osmotically balanced by substituting [Na^+].

Live imaging. Arclight, Archon1, pHluorin or iGluSnFr slices were placed in a submersion chamber (Siskiyou or Warner), held in place with small gold wires and perfused with aCSF containing 20 µM DNQX (antagonist of AMPA receptors) and 50 µM APV (antagonist of NMDA receptors), equilibrated with 95% O_2/5% CO_2 and circulated at 2 ml min^{-1} at 34 °C. A tungsten concentric bipolar stimulating electrode (FHC, Bowdoin) was placed in the deep cortical layers while the upper cortical layers were imaged with a ×60 or ×20 water-immersion objective (for iGluSnFr) (LUMPLANFL, Olympus) on a custom Prior Open-Scope with X-light V2 spinning-disk confocal microscope (Crest-optics, 89North LDI). Stimulus intensities were not significantly different between Arclight imaging and whole-cell astrocyte recordings, but Archon imaging used slightly increased stimulus intensities on average (0.19 ± 0.01, 0.26 ± 0.02 and 0.16 ± 0.01 mA for Arclight, Archon and whole-cell patch-clamp, respectively). One-way analysis of variance (ANOVA), $P=6.4\times10^{-5}$ for Archon versus Arclight or $P=1.1\times10^{-5}$ whole-cell patch-clamp, and $P=0.26$ for Arclight versus whole-cell patch-clamp; $n=62$, 39 and 22, respectively). For two-stimulator experiments, a second identical tungsten-stimulating electrode was placed in the upper cortical layers ~450 µm from the site of imaging. The 100-µs stimulus pulses were generated through a stimulus isolator ISO-Flex (A.M.P.I.). Stimulus intensity was set at twice the resolvable threshold stimulation, and imaging was performed using either a Prime95B (Photometrics) or Zyla5.5 (Andor) camera, with 12-bit digitization, 10-ms rolling shutter mode for 100-Hz temporal resolution and illuminated by a 470- or 640-nm laser (89North) or LED (iGluSnFr, CoolLED) controlled by MicroManager[42]. Arclight and Archon1 were imaged in confocal mode, using restricted illumination for enhanced laser illumination intensity, while iGluSnFr was imaged in bypass (epifluorescence) mode using a GFP filter cube (Chroma). Stimulus responses were imaged in sequences of five repetitions of one stimulation, followed by five and ten stimulations at 100 Hz and a no-stimulus control trace. This sequence was repeated at least five times for each slice. For each stimulus a 1-s burst was acquired (100 frames). For iGluSnFr imaging, the same sequencing was used except that each stimulus condition was repeated once only in each sequence. Drugs were washed on for 5 min before recommencing imaging.

For confocal line-scanning microscopy (CLSM) imaging, slices from mice infected with Arclight or Archon, in addition to GFAP-tdTomato to fill astrocytes, were placed on an Olympus BX51 microscope with a ThorLabs Laser Scanning Confocal attachment. Slices were imaged with an Olympus ×20/1.0 numerical aperture water-immersion objective (LUMPLANFL, Olympus) with 488- and 561-nm laser lines. Regions of 64 × 128 pixels at 318 nm per pixel were imaged at 43.5 Hz. Ten stimuli at 100 Hz and no-stimulation traces were interlaced.

Astrocyte whole-cell recordings. Astrocyte whole-cell recordings were performed similarly to previous studies[25,43,44]. Briefly, whole-cell patch-clamp recordings were made in an identical setup to live-cell imaging. Astrocytes were identified by morphology (small, round cell bodies), membrane properties and SR-101 labeling[38] as imaged with a Cy3 filter cube (excitation 560/40 nm, emission 630/75 nm, Chroma). Astrocyte internal solution contained the following (in mM): 120 potassium gluconate, 20 HEPES, 10 EGTA, 2 MgATP and 0.2 NaGTP. Borosilicate pipettes (4–12 MΩ) were used to establish whole-cell patch-clamp recordings with a Multiclamp 700B patch-clamp amplifier (Molecular Devices), sampled at 10 kHz using pClamp software. Once a whole-cell recording was established, cells were confirmed as astrocytes based on their passive membrane properties, low membrane resistance and hyperpolarized resting membrane potential. Slices were perfused with aCSF containing 20 µM DNQX and 50 µM APV, which was oxygenated and circulated at 2 ml min^{-1} and 34 °C. Stimulus responses were activated as for live-cell imaging above. In voltage-clamp mode, whole-cell, patch-clamped astrocytes were maintained at −80 mV. Changes in V_m were recorded in current-clamp mode while glutamate transporter currents were recorded in voltage-clamp mode. iGluSnFr decays were fit as previously, with monoexponential decay functions[6].

NR2A-NMDA receptor excitatory postsynaptic current current recording. NMDA receptor excitatory postsynaptic currents were recorded similarly to previous studies[6,44]. Briefly, whole-cell, patch-clamp recordings were made in an identical setup to live-cell imaging, with aCSF containing gabazine (10 µM), DNQX (20 µM), ifenprodil (5 µM) and D-serine (30 µM). Neurons identified by morphology in layer II/III of the cortex were whole-cell patch-clamped using 2–5-MΩ borosilicate glass electrodes containing the following (in mM): 120 D-gluconic acid, 120 CsOH, 10 HEPES, 10 EGTA, 0.5 $CaCl_2$, 20 TEA, 2 MgATP and 0.2 NaGTP. In voltage-clamp mode, neurons were held at +40 mV to relieve Mg^{2+} blocking of NMDA receptors and allowed to stabilize. NMDA currents were then evoked identically to the live-cell imaging above. Access resistance was monitored throughout the experiment, and cells with >25% change were excluded from analysis. NMDA current decays were fit as previously, with monoexponential decay functions[6].

Controlled cortical impact model. We utilized a controlled cortical impact (CCI) model of traumatic brain injury as a positive control for reactive astrocytosis. CCI was performed as previously described[45,46]. Briefly, 10- to 14-week-old male mice were anesthetized with inhaled isoflurane in oxygen (4% for induction, 2% for maintenance). Following placement in a stereotaxic frame, a 5-mm craniectomy was performed over the left somatosensory cortex and the skull flap removed. Impact was performed with a Leica Benchmark Stereotaxic Impactor using a 3-mm-diameter piston, 3.5 m s^{-1} velocity, 400-ms dwell time and 1-mm depth. After the CCI procedure, sutures were used to close the incision.

Immunofluorescence. Fixed mouse brains were prepared by transcardial perfusion with 4% paraformaldehyde. Fixed brains were sectioned at 30 µm using a ThermoFisher Microm HM 525 cryostat. Brain sections were blocked with blocking buffer (5% normal goat serum and 1% bovine serum albumin in PBS) for 1 h at room temperature. NEUN (1:500, no. MAB377B, Millipore), GFP (1:500, no. ab13970, Abcam), glutamine synthase (1:500, no. MAB302, Millipore), Kir4.1 (1:200, no. APC-035, Alomone), GFAP (1:500, no. ab7260, Abcam) and Sox9 (1:500, no. ab5535, Sigma) were diluted in PBS with 2% Triton X-100 and 5% blocking buffer. Cortical sections were incubated with diluted primary antibodies overnight at 4 °C. Secondary antibodies (goat anti-rabbit Cy3 and goat anti-chicken FITC, Jackson ImmunoResearch Laboratories) were diluted 1:500 in PBS with 5% blocking buffer and added to cortical sections for 2 h at room temperature. Slices were imaged with either a Nikon A1R or Leica SP8 confocal microscope. Slices from three mice were stained for all experiments, with between two and four slices per mouse visualized.

Immunoblot. C57 mice infected with either Kir4.1 or control virus were rapidly decapitated. Brains were removed and cortex was dissected. Microdissected regions were placed in ice-cold sodium phosphate-based lysis buffer (20 mM sodium phosphate, 1% SDS and protease inhibitors (Pierce Protease Inhibitor Tablets, no. A32963)) and sonicated for 14 s. Tissue homogenates were centrifuged for 7 min at 14,000*g* at 4 °C. Following BCA protein assay (ThermoFisher), equal amounts of protein (15 µg) were heated to 60 °C for 15 min in DTT-based reducing reagent (NuPAGE Sample Reducing Agent and LDS Sample buffer, ThermoFisher, nos. NP0009 and NP0007). Prepped samples were electrophoresed on gels, 10% MP TGX, 12 W and 20 µl of precast gels (BioRad) for 1.5 h at 150 V at room temperature. Protein was transferred onto nitrocellulose membranes (Li-Cor) at 30 V overnight at 4°C using two layers of sponges and cold packs. Membranes were blocked in 5% milk (nonfat dried milk, Sigma, no. M7409-1BTL) in Tris-buffered saline with Tween (T-BST) with shaking for 1 h at room temperature. Membranes were incubated, with shaking, in TBS-T, with the following primary antibodies: Kir4.1 (1:400) (anti-Kir4.1 (KCNJ10) Antibody Alomone, no. APC-035). Membranes were then washed for 3 × 10 min in TBS-T and incubated, with shaking, with secondary antibodies, prepared in the same solution as primary antibodies: horseradish peroxidase-linked secondary antibody and goat anti-rabbit (1:10,000; anti-Rabbit IgG (whole-molecule)-peroxidase antibody, Sigma, no.

A6154) for 2 h at room temperature. Membranes were then washed for 3 × 10 min in TBS-T and for 5 min in TBS before imaging with an Odyssey scanner. Bands were quantified using the NIH-approved protocol in ImageJ and normalized to beta-actin.

Astrocyte territory segmentation. Segmentation of astrocytes labeled with tdTomato was performed in Imaris (Bitplane, Oxford Instruments) using the surface plug-in in a semiautomated manner. Individual astrocytes, their overall territory volume and volume occupied by the soma were carefully segmented and quantified using a watershed algorithm incorporated into the plug-in, which was applied to the tdTomato channel. The resulting segmented volume was also used as a three-dimensional mask to visualize and quantify the intensity of the Arclight or Archon channel within astrocytic territory.

Imaging analysis. Spinning-disk confocal analysis was performed using MATLAB (The MathWorks) and Origin (Originlab). Following imaging, all acquired images from individual slices were aligned using the NoRMCorre algorithm[47]. Following alignment, average $\Delta F/F_0$ images were generated and corrected for background fluorescence using the no-stimulus and individual stimulus conditions. ROIs were generated using Cell Sort PCA/ICA algorithms[15] based on a spatial and temporal Gaussian (one pixel per frame kernel)-filtered ten stimulation at 100-Hz $\Delta F/F_0$ images. The analysis was given the full-sweep duration and was blind to stimulus timing. ROIs were spatially constricted in size to at least two pixels. PCA/ICA identified the stimulus response from the full sweep and generated ROIs found throughout the image, had a nonrandom distribution and had a kinetic profile similar to the $\Delta F/F_0$ signal seen across the entire image. To validate the approach, we compared ROIs identified using PCA/ICA to an alternative approach in which pixels with the highest $\Delta F/F_0$ at the end of the stimulus were selected. The number of pixels selected was comparable to that selected by PCA/ICA. This approach identified the noisiest pixels at the time of stimulation, had no kinetic similarity to the signal detected across the entire image and was randomly distributed in space (Supplementary Fig. 1). Based on this comparison, PCA/ICA analysis was far superior. $\Delta F/F_0$ measures are susceptible to distortion if basal fluorescence (F_0) is very low. This concern is most relevant in regard to Archon GEVI, which has a very dim baseline, while Arclight GEVI is bright at baseline. To test whether the ROIs selected using PCA/ICA were biased toward low F_0 values, distorting $\Delta F/F_0$ measurements, we compared ROI $\Delta F/F_0$ to F_0, on a hotspot-by-hotspot basis. This showed no correlation for either GEVI (Supplementary Fig. 2). Lastly, the PCA/ICA algorithm detected similar responses for either Arclight or Archon1 (but in opposite directions), because Arclight is bright at baseline and reduces fluorescence while Archon is dim at baseline and increases in brightness. Together this supports the premise that the PCA/ICA-based approach to ROI detection is valid. Kymographs were generated by upsampling ROIs tenfold to enable subpixel alignment based on the center of mass of the detected ROI. Only ROIs of area less than ten pixels were included, to avoid merged ROIs. For FWHM measurements, individual slice kymographs were fit with a two-dimensional (2D) Gaussian function (MATLAB) to calculate FWHM. GEVI decays were quantified by calculation of $T_{1/2}$ based on the end of the stimulus.

Following CLSM imaging, all acquired images were aligned using the NoRMCorre algorithm and $\Delta F/F_0$ images were created. ROIs of three pixels in diameter were placed on all discernable hotspots, in addition to somas and primary processes (based on tdTomato fluorescence) and a full-field ROI using FIJI/ImageJ[48]. Traces from each ROI were manually inspected and averaged for each slice. Additionally, centroids of each ROI were calculated and used to analyze distance from the soma centroid for individual astrocytes. Individual hotspots were fit with a 2D Gaussian peak function to establish the primary axis, calculate FWHM and rotate-align all hotspots, followed by NoRMCorre alignment. Based on peak location, half distributions were fit with 2D Gaussians (MATLAB) to calculate individual half-axes σ, and skewing of distributions calculated.

Pharmacology. Unless otherwise noted, all salts and glucose were obtained from Sigma-Aldrich. Drugs used in the study and their concentration were: APV (NMDA antagonist, 50 µM, Tocris Bioscience)[49]; DNQX (AMPA antagonist, 20 µM, Sigma)[50]; D-Serine (NMDA coagonist, 30 µM, Sigma)[51]; gabazine (6-imino-3-(4-methoxyphenyl)-1(6*H*)-pyridazinebutanoic acid hydrobromide, $GABA_A$ antagonist, 10 µM, Tocris Bioscience)[52]; Ifenprodil ((1*S**,2*S**)-*threo*-2-(4-benzylpiperidino)-1-(4-hydroxyphenyl)-1-propanol hemitartrate; NR2B antagonist, 5 µM, Tocris Bioscience)[53]; TFB-TBOA (EAAT antagonist, 1 µM, Tocris Bioscience)[54]; and TTX (Na_V channel antagonist, 1 µM, Sigma). Drugs were kept as 1,000× stock in either H_2O (APV, D-serine, gabazine, ifenprodil, TTX) or DMSO (DNQX, DPCPX, TFB-TBOA).

Statistics and reproducibility. Individual statistical tests are noted throughout the manuscript/figure legends but, briefly, most analyses were performed with two-way ANOVA or two-way repeated-measures ANOVA, both with Tukey's post test, to examine the significance of the treatment group. For brevity, additional statistical tests of individual stimulus conditions were not performed. No statistical methods were used to predetermine sample sizes, but our sample sizes are similar to those reported in previous publications[6,55,56]. Data distribution was assumed to be normal, but this was not formally tested. Data collection and analysis were not performed blind to the conditions of the experiments, because most experiments had paired designs making blinding impractical. Most experiments were of paired design, making randomization impractical. All data that passed quality control (access resistance, stability and so on) are included in analyses.

Reporting Summary. Further information on research design is available in the Nature Research Reporting Summary linked to this article.

Data availability

Source data are provided with this paper. The datasets generated during and analyzed during the current study are available from the corresponding author on request.

Code availability

All computer code used to collect and analyze data are available from the corresponding author on request.

References

38. Nimmerjahn, A., Kirchhoff, F., Kerr, J. & Helmchen, F. Sulforhodamine 101 as a specific marker of astroglia in the neocortex in vivo. *Nat. Methods* **1**, 31–37 (2004).
39. Frankenhaeuser, B. & Hodgkin, A. L. The action of calcium on the electrical properties of squid axons. *J. Physiol.* **137**, 218–244 (1957).
40. Hille, B., Woodhull, A. M. & Shapiro, B. I. Negative surface charge near sodium channels of nerve: divalent ions, monovalent ions, and pH. *Philos. Trans. R. Soc. Lond. B Biol. Sci.* **270**, 301–318 (1975).
41. Isaev, D. et al. Surface charge impact in low-magnesium model of seizure in rat hippocampus. *J. Neurophysiol.* **107**, 417–423 (2012).
42. Edelstein, A. D. et al. Advanced methods of microscope control using muManager software. *J. Biol. Methods* **1**, e10 (2014).
43. Armbruster, M., Hampton, D., Yang, Y. & Dulla, C. G. Laser-scanning astrocyte mapping reveals increased glutamate-responsive domain size and disrupted maturation of glutamate uptake following neonatal cortical freeze-lesion. *Front. Cell. Neurosci.* **8**, 277 (2014).
44. Hanson, E. et al. Astrocytic glutamate uptake is slow and does not limit neuronal NMDA receptor activation in the neonatal neocortex. *Glia* **63**, 1784–1796 (2015).
45. Cantu, D. et al. Traumatic brain injury increases cortical glutamate network activity by compromising GABAergic control. *Cereb. Cortex* **25**, 2306–2320 (2014).
46. Koenig, J. B. et al. Glycolytic inhibitor 2-deoxyglucose prevents cortical hyperexcitability after traumatic brain injury. *JCI Insight* https://doi.org/10.1172/jci.insight.126506 (2019).
47. Pnevmatikakis, E. A. & Giovannucci, A. NoRMCorre: an online algorithm for piecewise rigid motion correction of calcium imaging data. *J. Neurosci. Methods* **291**, 83–94 (2017).
48. Schindelin, J. et al. Fiji: an open-source platform for biological-image analysis. *Nat. Methods* **9**, 676–682 (2012).
49. Evans, R. H., Francis, A. A., Jones, A. W., Smith, D. A. & Watkins, J. C. The effects of a series of omega-phosphonic alpha-carboxylic amino acids on electrically evoked and excitant amino acid-induced responses in isolated spinal cord preparations. *Br. J. Pharmacol.* **75**, 65–75 (1982).
50. Honore, T. et al. Quinoxalinediones: potent competitive non-NMDA glutamate receptor antagonists. *Science* **241**, 701–703 (1988).
51. Le Meur, K., Galante, M., Angulo, M. A. C. & Audinat, E. Tonic activation of NMDA receptors by ambient glutamate of non-synaptic origin in the rat hippocampus. *J. Physiol.* **580**, 373–383 (2007).
52. Heaulme, M. et al. Biochemical characterization of the interaction of three pyridazinyl-GABA derivatives with the GABAA receptor site. *Brain Res.* **384**, 224–231 (1986).
53. Williams, K. Ifenprodil discriminates subtypes of the N-methyl-D-aspartate receptor: selectivity and mechanisms at recombinant heteromeric receptors. *Mol. Pharmacol.* **44**, 851–859 (1993).
54. Shimamoto, K. et al. Characterization of novel L-threo-beta-benzyloxyaspartate derivatives, potent blockers of the glutamate transporters. *Mol. Pharmacol.* **65**, 1008–1015 (2004).
55. Hanson, E. et al. Tonic activation of GluN2C/GluN2D-containing NMDA receptors by ambient glutamate facilitates cortical interneuron maturation. *J. Neurosci.* **39**, 3611–3626 (2019).
56. Armbruster, M., Dulla, C. G. & Diamond, J. S. Effects of fluorescent glutamate indicators on neurotransmitter diffusion and uptake. *eLife* **9**, e54441 (2020).

Acknowledgements

We thank members of the Dulla, Haydon and Rios laboratories, and J. Raimondo and J. Diamond for helpful comments on the manuscript. We thank Y. Yang (Tufts) for EAAT2-tdTomato mice. We thank L. Looger (UCSD), V. Pieribone (Yale), B. Khakh (UCLA) and S. Grinstein (University of Toronto) for making available plasmids and constructs. This work was supported by the NIH (nos. NS113499, NS104478 and NS100796 to C.G.D.; MH117042 to AEC).

Author contributions

M.A. oversaw conceptualization, methodology, investigation, formal analysis, data curation, visualization and writing of the original draft. S.N. carried out investigation, formal analysis, writing and review and editing. J.P.G., M.S. and E.K. performed investigation. Y.A. carried out methodology and investigation. P.G.H., A.E.C. and E.S.B. were responsible for resources and methodology. C.G.D. oversaw conceptualization, formal analysis, visualization, supervision, funding acquisition, project administration, resources and writing of the original draft.

Competing interests

The authors declare no competing interests.

Additional information

Extended data is available for this paper at https://doi.org/10.1038/s41593-022-01049-x.

Supplementary information The online version contains supplementary material available at https://doi.org/10.1038/s41593-022-01049-x.

Correspondence and requests for materials should be addressed to Moritz Armbruster or Chris G. Dulla.

Peer review information *Nature Neuroscience* thanks Yukiko Goda, Michelle L. Olsen and the other, anonymous, reviewer(s) for their contribution to the peer review of this work.

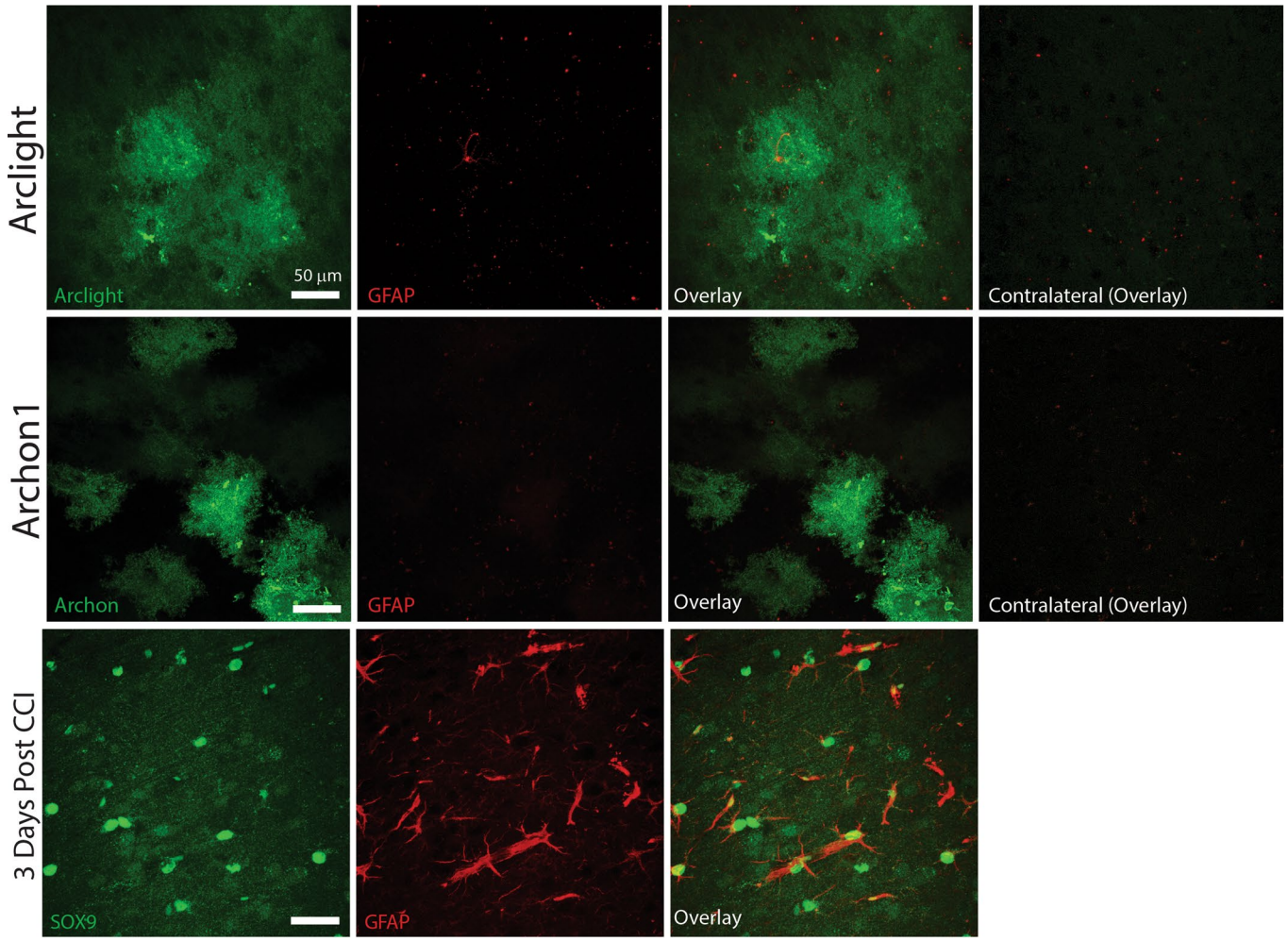

Extended Data Fig. 1 | GEVI expression does not induce reactive astrocytosis. Representative confocal IHC images stained for GFAP in Arclight infected and Archon1-EGFP (EGFP fluorescence shown) infected cortices. Additionally, staining in matched uninfected contralateral cortex. Neither GEVI infected or uninfected contralateral cortex shows high GFAP levels, indicative of a lack of reactive astrocytosis. In order to verify the sensitivity of our GFAP antibody, we stained slices 3 days following controlled cortical impact, a robust model of traumatic brain injury. In this positive control, astrocytes are labeled with the astrocyte specific marker Sox9 and shows high levels of GFAP staining and astrocytosis. Scalebar = 50 µm.

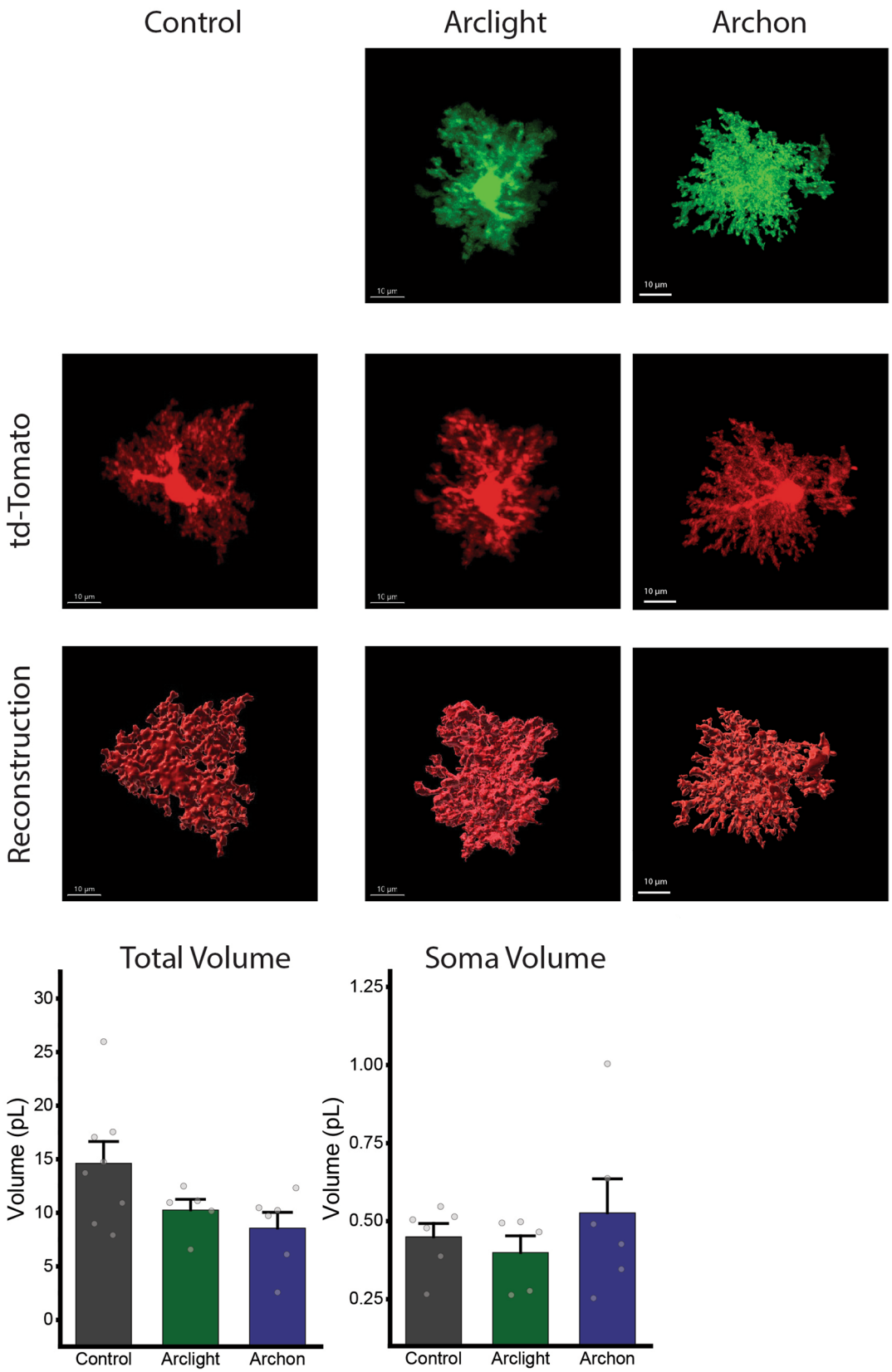

Extended Data Fig. 2 | GEVI expression does not change astrocyte morphology. Example confocal sections and reconstruction of the astrocyte cell-fill reporter tdTomato either uninfected controls (left column), Arclight infected (middle column), or Archon infected (right column). No significant changes were observed in total astrocyte volume or soma volume between control or GEVI infected astrocytes. N= 8 control, 5 Arclight, 6 Archon astrocytes. One way ANOVA Control v Arclight $p = 0.23$, Control v Archon $p = 0.058$, Arclight v Archon $p = 0.81$. All panels: Error bars = Standard error of the mean.

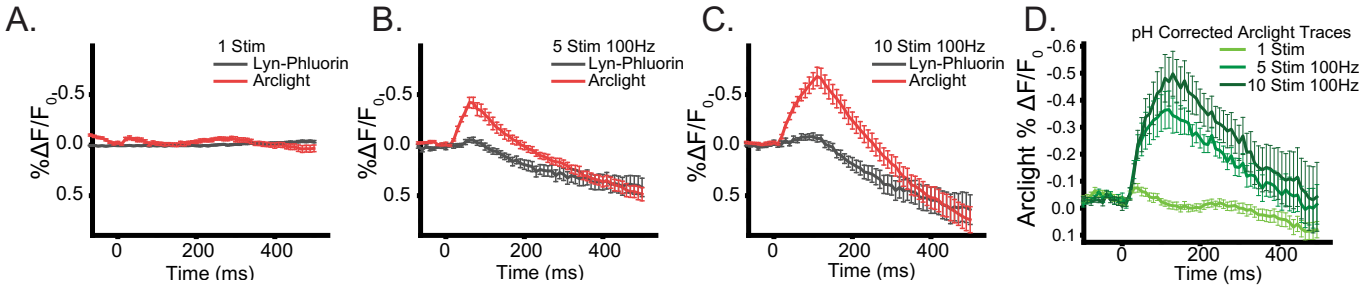

Extended Data Fig. 3 | Correcting pH transients. Average pH transients (Lyn-pHluorin) and Arclight GEVI responses to A) 1 Stim, B) 5 Stimuli at 100Hz, C) 10 Stimuli at 100Hz. D) The GEVI decays are corrected for the pH changes using the difference in the Arclight and pHluorin traces. n = 9 Slices/ 3 mice (pHluorin). n = 17 slices/6 mice (Arclight). All panels: Error bars = Standard error of the mean.

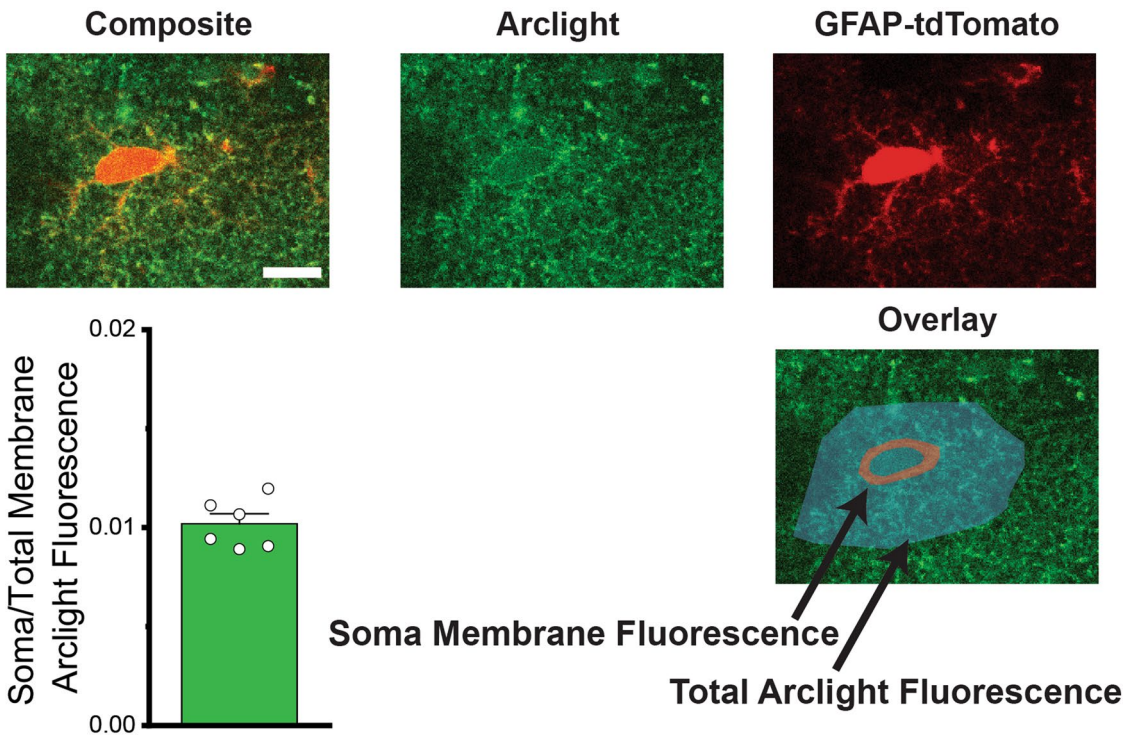

Extended Data Fig. 4 | Astrocyte membrane probes primarily localize to astrocyte process rather than soma. Example confocal images from a 3D Z-stack of astrocyte targeted Arclight (a membrane targeted GEVI) and an astrocyte cell fill (GFAP-tdTomato). We subsequently quantified the Arclight fluorescence originating from the soma membrane compared to the total astrocyte Arclight fluorescence in all Z-sections. Soma fluorescence represents 1.0 ± 0.0005% of the total Arclight fluorescence N = 6 astrocytes. Scale bar = 10 μm.

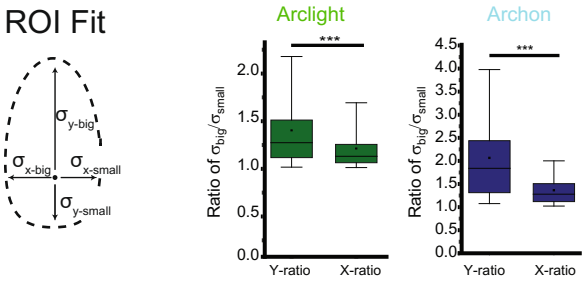

Extended Data Fig. 5 | Confocal Laser Scanning Microscopy shows ROI hotspots have skewed distributions. Half of individual ROI hotspots from Fig. 3g,h, are fit with 2D gaussians to determine one-sided standard deviations for X and Y- axis. Both Arclight and Archon show significantly more skewed fluorescence distribution along the Y-axis. Box-Whisker plot, Box = 25, 50, 75th percentile, whiskers = 5-95th percentile, square = mean. *** = $p < 0.001$. N= 1109 ROIs (Arclight, p = 1.1E-30) and N=104 ROIs (Archon p = 3.3E-11).

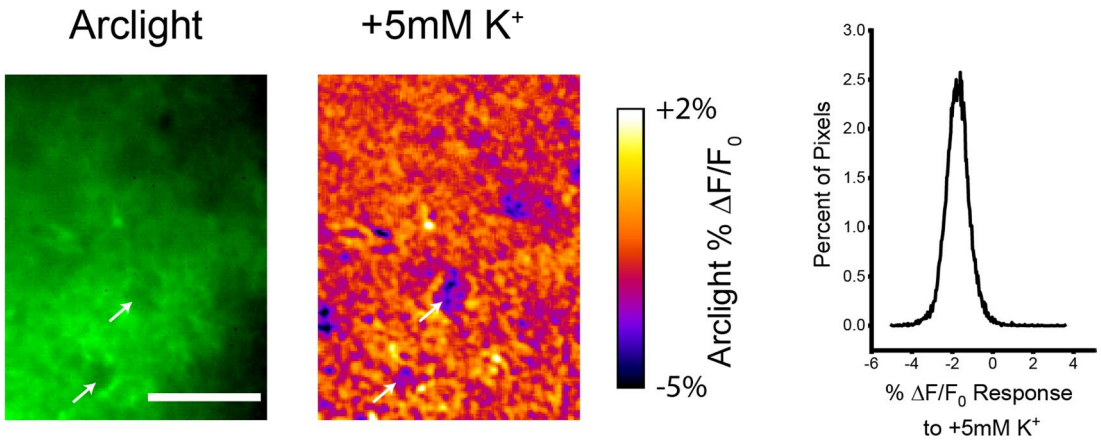

Extended Data Fig. 6 | K^+ wash-on calibration induces uniform depolarization. Example image of Arclight (scale bar = 30 μm) and response image to +5mM K^+ wash-on, shows largely uniform voltage response across the field. Outliers, such as those highlighted with white arrows, tend to be areas excluding the Arclight sensor such as somas, or blood vessels. Distribution of pixel responses to +5mM K^+ shows a uniform distribution of depolarization responses.

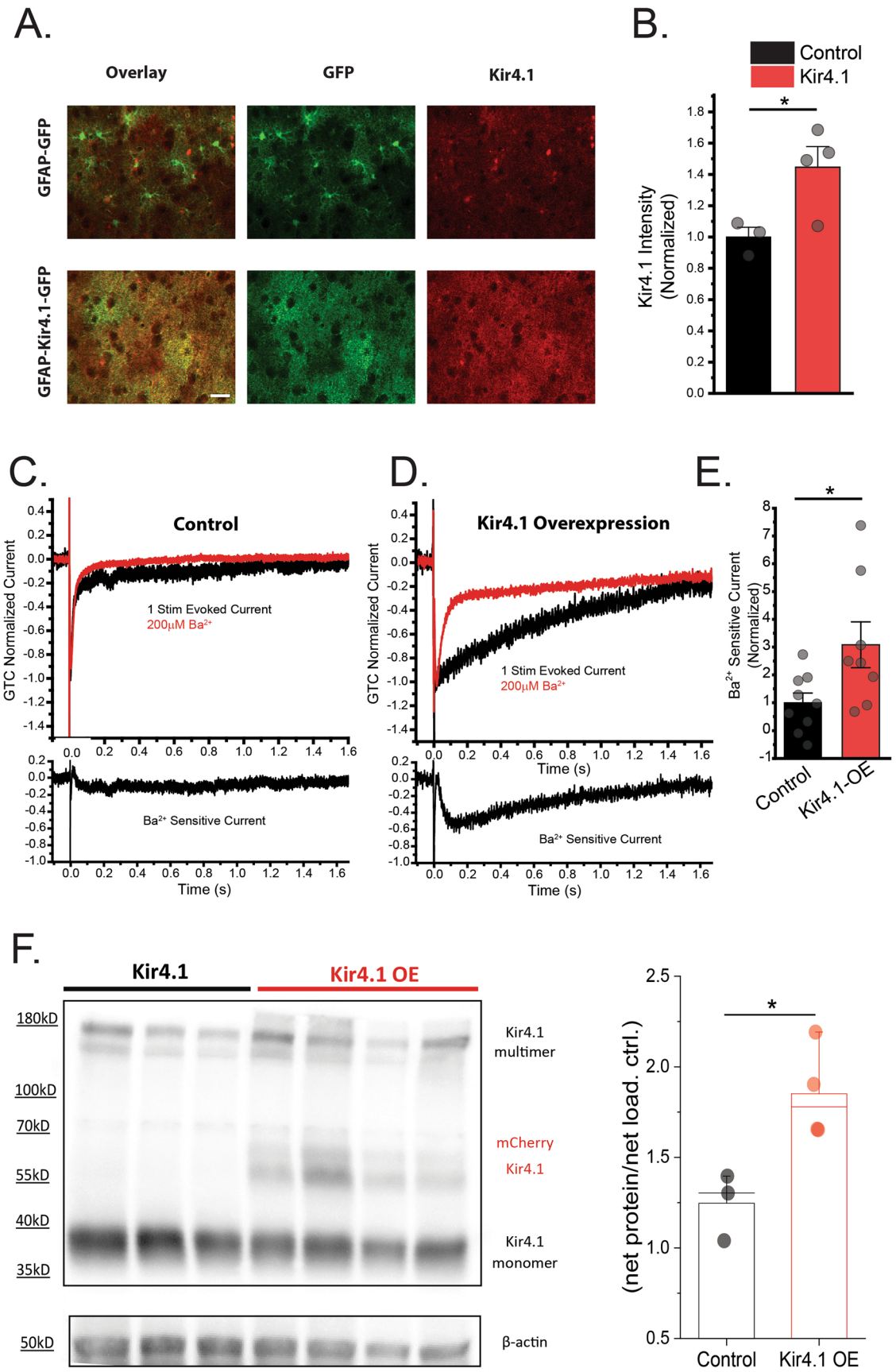

Extended Data Fig. 7 | See next page for caption.

Extended Data Fig. 7 | Kir4.1 Overexpression. A) Confocal example image of immunofluorescence staining of Kir4.1 in Kir4.1 overexpression (Kir4.1-OE), (AAV5-GFAP-Kir4.1-EGFP) or control (AAV5-GFAP-GFP) infected cortex. B) Quantification of widefield Kir4.1 IHC staining shows significantly enhanced Kir4.1 staining. Scale bar = 50 μm. Two-sample t-test, n=3, 4 mice, $p = 0.038$. C, D) Astrocyte whole-cell voltage clamp shows enhanced Ba^{2+} (Kir4.1 inhibitor) sensitive currents in Kir4.1-OE compared to control-infected cortex. 9 cells/3 mice each. E) Ba^{2+}- sensitive currents are significantly increase in Kir4.1-OE astrocytes, $p = 0.028$. F) Western blot quantification of Kir4.1-OE (AAV5-GFAP=Kir4.1-mCherry), shows significantly increased Kir4.1 protein compared to control virus (AAV5-GFAP-tdTomato). $p = 0.049$ * = $p < 0.05$ All panels: Error bars = Standard error of the mean.

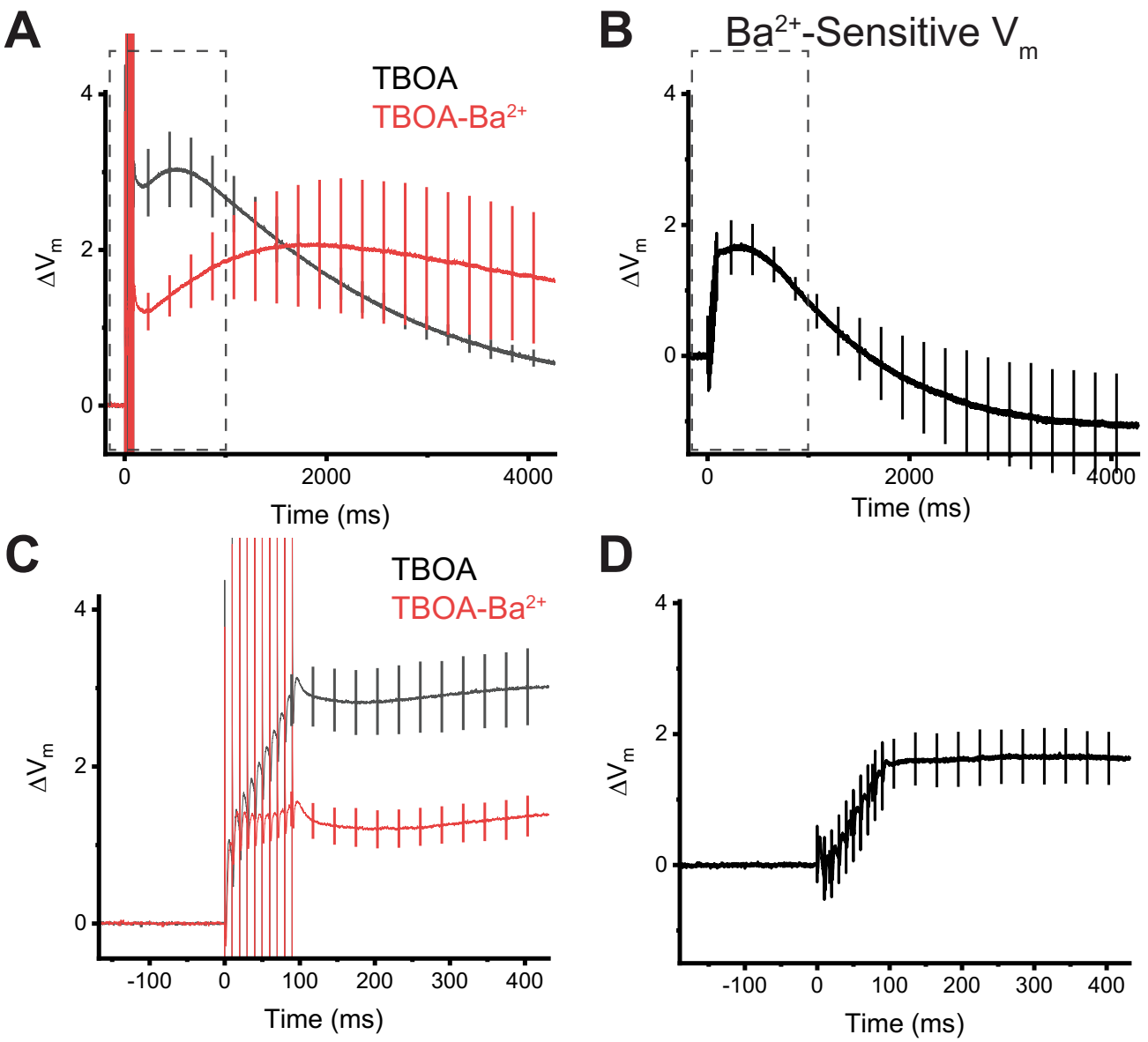

Extended Data Fig. 8 | Kir4.1 depolarizes astrocyte soma during neuronal activity. Astrocyte-whole cell current clamp recordings were made in the cortex to measure somatic V_m. In order to isolate the effects of Kir4.1 on astrocyte V_m during neuronal activity, glutamate transporter activity was blocked with TFB-TBOA and responses to 10 stimuli at 100Hz were recorded before and after blockade of Kir4.1 with Ba^{2+}. A) Average paired traces before (black) and after (red) inhibition of Kir4.1 with Ba^{2+}, and B) the Ba^{2+}-sensitive ΔV_m. These recordings show that Kir4.1 depolarizes astrocyte soma during neuronal activity. C and D) Expanded time scale (dashed boxes in A & B) to show V_m during stimulus. N = 5 cells. All panels: Error bars = Standard error of the mean.

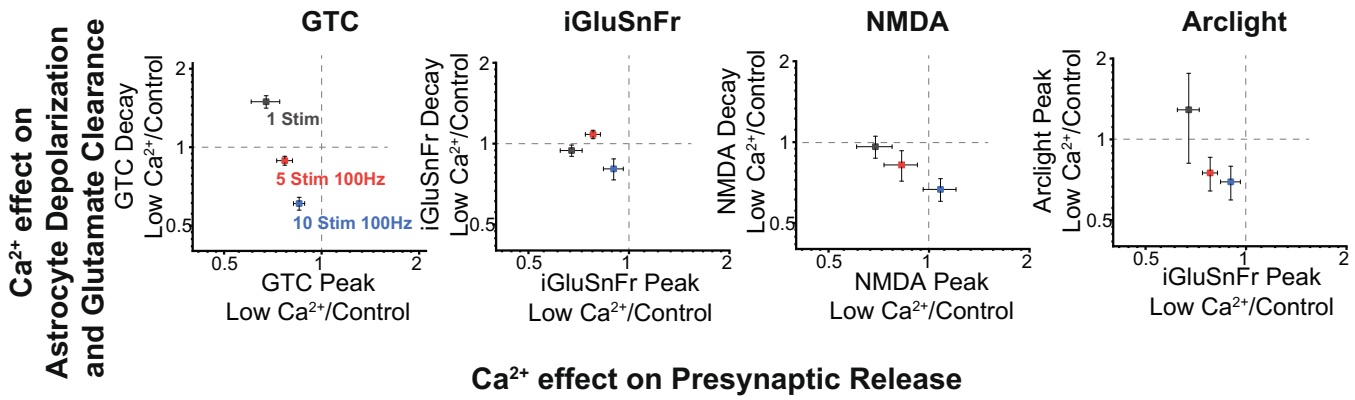

Extended Data Fig. 9 | The effects of low Ca^{2+} on presynaptic release do not correlate with the effects on glutamate clearance and astrocyte depolarization. Utilizing data from Figs. 6, 7, and Extended Data Fig. 10 we plotted the effects of Low Ca^{2+} aCSF on presynaptic release (x-axis) and glutamate clearance/astrocyte depolarization (y-axis) for 1, 5, and 10 stimuli at 100Hz. In each condition, Low Ca^{2+} is normalized to control. Dashed lines represent no change from control. Left of the dashed line on the x-axis represents a reduction in presynaptic release (as assayed by GTC, iGluSnFr, or NMDA peak amplitude). Beneath the dashed line represents an enhanced glutamate clearance/reduced depolarization (as assayed by GTC/iGluSnFr/NMDA decays and Arclight peaks). 1 Stim responses (grey) shows the largest change in presynaptic release, with the smallest effect on glutamate clearance/depolarization. 10 Stimuli at 100Hz (blue) shows the smallest presynaptic release effect with the largest glutamate clearance/depolarization effect.

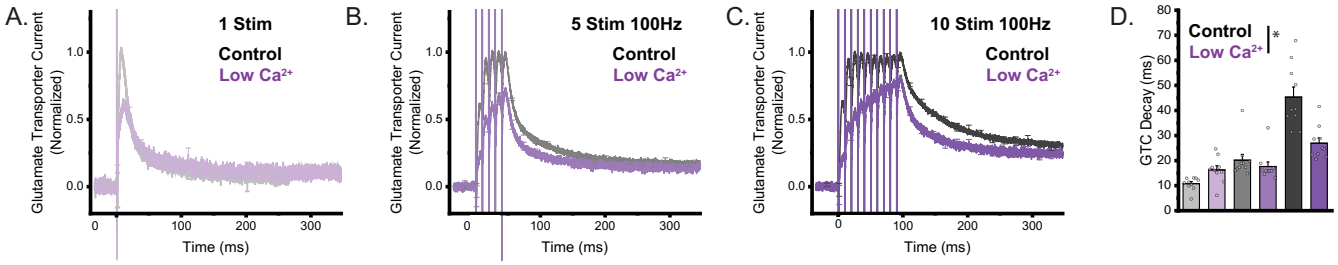

Extended Data Fig. 10 | Low Ca^{2+} Glutamate Transporter Currents. Glutamate transporter currents were recorded from astrocytes with Control or Low Ca^{2+} aCSF, showing enhanced glutamate clearance following trains of stimulation. Two way repeated measures ANOVA * = $p<0.05$. n = 10 cells/3 mice, $p = 0.046$. All panels: Error bars = Standard error of the mean.

nature portfolio

Corresponding author(s): Moritz Armbruster, Chris Dulla

Last updated by author(s): Jan 21, 2022

Reporting Summary

Nature Portfolio wishes to improve the reproducibility of the work that we publish. This form provides structure for consistency and transparency in reporting. For further information on Nature Portfolio policies, see our Editorial Policies and the Editorial Policy Checklist.

Statistics

For all statistical analyses, confirm that the following items are present in the figure legend, table legend, main text, or Methods section.

n/a	Confirmed	
☐	☒	The exact sample size (*n*) for each experimental group/condition, given as a discrete number and unit of measurement
☐	☒	A statement on whether measurements were taken from distinct samples or whether the same sample was measured repeatedly
☐	☒	The statistical test(s) used AND whether they are one- or two-sided *Only common tests should be described solely by name; describe more complex techniques in the Methods section.*
☒	☐	A description of all covariates tested
☐	☒	A description of any assumptions or corrections, such as tests of normality and adjustment for multiple comparisons
☐	☒	A full description of the statistical parameters including central tendency (e.g. means) or other basic estimates (e.g. regression coefficient) AND variation (e.g. standard deviation) or associated estimates of uncertainty (e.g. confidence intervals)
☐	☒	For null hypothesis testing, the test statistic (e.g. *F*, *t*, *r*) with confidence intervals, effect sizes, degrees of freedom and *P* value noted *Give P values as exact values whenever suitable.*
☒	☐	For Bayesian analysis, information on the choice of priors and Markov chain Monte Carlo settings
☒	☐	For hierarchical and complex designs, identification of the appropriate level for tests and full reporting of outcomes
☒	☐	Estimates of effect sizes (e.g. Cohen's *d*, Pearson's *r*), indicating how they were calculated

Our web collection on statistics for biologists contains articles on many of the points above.

Software and code

Policy information about availability of computer code

Data collection	Micromanager (https://micro-manager.org/ doi:10.14440/jbm.2014.36); pClamp11 (Axon Instruments);
Data analysis	Matlab 2020(Mathworks); CellSort 1.1 DOI: 10.1016/j.neuron.2009.08.009; NoRMCorre DOI: 10.1016/j.jneumeth.2017.07.031; Origin2019b (OriginLab)

For manuscripts utilizing custom algorithms or software that are central to the research but not yet described in published literature, software must be made available to editors and reviewers. We strongly encourage code deposition in a community repository (e.g. GitHub). See the Nature Portfolio guidelines for submitting code & software for further information.

Data

Policy information about availability of data

All manuscripts must include a data availability statement. This statement should provide the following information, where applicable:

- Accession codes, unique identifiers, or web links for publicly available datasets
- A description of any restrictions on data availability
- For clinical datasets or third party data, please ensure that the statement adheres to our policy

The datasets generated during and analyzed during the current study are available from the corresponding author on request.

Field-specific reporting

Please select the one below that is the best fit for your research. If you are not sure, read the appropriate sections before making your selection.

☒ Life sciences ☐ Behavioural & social sciences ☐ Ecological, evolutionary & environmental sciences

For a reference copy of the document with all sections, see nature.com/documents/nr-reporting-summary-flat.pdf

Life sciences study design

All studies must disclose on these points even when the disclosure is negative.

Sample size	No statistical methods were used to predetermine sample sizes. >3 mice were used for each experiment, and greater number of slices, based on previous methods (Armbruster et al J. Neuroscience 2016)
Data exclusions	No data points were excluded from the study.
Replication	The study was designed to utilize two distinct and independent GEVI sensors in order to ensure reproducibility, and whenever possible key findings were tested using both the Arclight and Archon sensors.
Randomization	For paired experiments (Drug washon), no randomization was possible. For unpaired experiments, mice were randomly assigned control or experimental viruses.
Blinding	The investigator was not blinded during data acquisition or analysis due to paired, drug-wash on design. Analysis was scripted to minimize bias effects.

Reporting for specific materials, systems and methods

We require information from authors about some types of materials, experimental systems and methods used in many studies. Here, indicate whether each material, system or method listed is relevant to your study. If you are not sure if a list item applies to your research, read the appropriate section before selecting a response.

Materials & experimental systems

n/a	Involved in the study
☐	☒ Antibodies
☒	☐ Eukaryotic cell lines
☒	☐ Palaeontology and archaeology
☐	☒ Animals and other organisms
☒	☐ Human research participants
☒	☐ Clinical data
☒	☐ Dual use research of concern

Methods

n/a	Involved in the study
☒	☐ ChIP-seq
☒	☐ Flow cytometry
☒	☐ MRI-based neuroimaging

Antibodies

Antibodies used	Primary: NEUN (MAB377B, Millipore), GFP (ab13970 Abcam), glutamine synthase (MAB302, Millipore), Kir4.1 (APC-035 Alomone), GFAP (ab7260 Abcam), Sox9 (ab5535 Sigma) Secondary: goat anti-rabbit Cy3, goat-anti chicken FITC, Jackson ImmunoResearch Laboratories, Anti Rabbit IgG peroxidase antibody Sigma A6154,
Validation	NEUN: "NeuN (cat. # MAB377B) staining pattern/morphology in rat cerebellum. Tissue pretreated with Citrate, pH 6.0. This lot of antibody was diluted to 1:100, using IHC-Select® Detection with HRP-DAB. Immunoreactivity is seen as nuclear staining in the neurons in the granular layer. Note that there is no signal detected in the nucleus of Purkinje cells." Millipore; Hippocampal staining patterns (Dulla lab); Co-stain with non-neuronal markers (GFAP) (Dulla lab). GFP: IF/WB of GFP positive vs negative cell lines (Abcam); IHC of GFP-negative brain slices (Dulla Lab); Glutamine synthase: "Reacts strongly with a single band on Western blots of sheep brain and rat brain. Glutamine synthetase, an enzyme that catalyzes the amination of glutamic acid to form glutamine, is found in mammals as an octamer of eight identical 45 kDa subunits. " Millipore Kir4.1: IHC on Kir4.1 cKO Djukic, B. et al. (2007) J. Neurosci. 27, 11354. GFAP: "Specifically recognizes mammalian GFAP on western blots and immunocytochemically. Detects a band of 55kDa corresponding to GFAP and also a GFAP derived 48kDa band." Abcam. Co-stains with other astrocyte makers EAAT2-tdtomato mouse line, EAAT2-antibodies (Dulla lab) Sox9: "Anti-Sox9 Antibody is a well characterized affinity purified Rabbit Polyclonal Antibody that reliably detects Transcription Factor Sox-9. This highly published antibody has been validated in IHC & WB." Sigma

Animals and other organisms

Policy information about studies involving animals; ARRIVE guidelines recommended for reporting animal research

Laboratory animals	C57BL/6 or EAAT2-tdtomato male and female mice (P30-45) were used
Wild animals	No wild animals were used in this study
Field-collected samples	No Field collected animals were used in this study
Ethics oversight	All animal protocols were approved by the Tufts Institutional Animal Care and Use Committee.

Note that full information on the approval of the study protocol must also be provided in the manuscript.